Check for updates

JGR Earth Surface

RESEARCH ARTICLE
10.1029/2023JF007481

Elastic Stress Coupling Between Supraglacial Lakes

Laura A. Stevens[1], Sarah B. Das[2], Mark D. Behn[3], Jeffrey J. McGuire[4], Ching-Yao Lai[5], Ian Joughin[6], Stacy Larochelle[7], and Meredith Nettles[7]

[1]Department of Earth Sciences, University of Oxford, Oxford, UK, [2]Department of Geology and Geophysics, Woods Hole Oceanographic Institution, Woods Hole, MA, USA, [3]Department of Earth and Environmental Sciences, Boston College, Chestnut Hill, MA, USA, [4]U.S. Geological Survey, Earthquake Science Center, Moffett Field, CA, USA, [5]Department of Geophysics, Stanford University, Stanford, CA, USA, [6]Applied Physics Lab, Polar Science Center, University of Washington, Seattle, WA, USA, [7]Lamont-Doherty Earth Observatory of Columbia University, Palisades, NY, USA

Abstract Supraglacial lakes have been observed to drain within hours of each other, leading to the hypothesis that stress transmission following one drainage may be sufficient to induce hydro-fracture-driven drainages of other nearby lakes. However, available observations characterizing drainage-induced stress perturbations have been insufficient to evaluate this hypothesis. Here, we use ice-sheet surface-displacement observations from a dense global positioning system array deployed in the Greenland Ice Sheet ablation zone to investigate elastic stress transmission between three neighboring supraglacial lake basins. We find that drainage of a central lake can place neighboring basins in either tensional or compressional stress relative to their hydro-fracture scarp orientations, either promoting or inhibiting hydro-fracture initiation beneath those lakes. For two lakes located within our array that drain close in time, we identify tensional surface stresses caused by ice-sheet uplift due to basal-cavity opening as the physical explanation for these lakes' temporally clustered hydro-fracture-driven drainages and frequent triggering behavior. However, lake-drainage-induced stresses in the up-flowline direction remain low beyond the margins of the drained lakes. This short stress-coupling length scale is consistent with idealized lake-drainage scenarios for a range of lake volumes and ice-sheet thicknesses. Thus, on elastic timescales, our observations and idealized-model results support a stress-transmission hypothesis for inducing hydro-fracture-driven drainage of lakes located within the region of basal cavity opening produced by the initial drainage, but refute this hypothesis for distal lakes.

Plain Language Summary Mass loss from the Greenland Ice Sheet is accelerating, partly due to increasing rates of ice flow to the ocean. Ongoing increases in ice-sheet surface melting play a complex role in this process: meltwater flows down through conduits and fractures to the ice-sheet bed, lubricates the ice-bed interface, and modulates ice-flow speeds on hourly to decadal timescales. Drainage of supraglacial lakes via hydro-fracture—water-driven fracture propagation—produces the highest rates of meltwater flux to the ice-sheet bed. The geographical range of lakes on the ice sheet has expanded in recent decades, but not all supraglacial lakes drain by hydro-fracture: whether a hydro-fracture-driven drainage occurs in any particular lake basin is controlled by the ice-sheet stress state. Here, we investigate whether one lake drainage can generate stress changes in neighboring lake basins that trigger hydro-fracture initiation. We find that the drainage of one lake does lead to tensional stresses that promote hydro-fracture initiation in a neighboring lake basin, but also that this initial lake drainage leads to a more compressive stress state that inhibits hydro-fracture initiation in a different neighboring lake basin.

Key Points:

- Drainage of one lake can place neighboring basins in tensional or compressional stress, promoting or inhibiting hydro-fracture initiation
- Tensional surface stresses are predominantly caused by basal cavity opening, with smaller contributions from basal slip
- The first-order control on elastic stress-coupling length scales is the region of the bed over which basal cavity opening occurs

Supporting Information:

Supporting Information may be found in the online version of this article.

Correspondence to:

L. A. Stevens,
laura.stevens@earth.ox.ac.uk

Citation:

Stevens, L. A., Das, S. B., Behn, M. D., McGuire, J. J., Lai, C.-Y., Joughin, I., et al. (2024). Elastic stress coupling between supraglacial lakes. *Journal of Geophysical Research: Earth Surface*, *129*, e2023JF007481. https://doi.org/10.1029/2023JF007481

Received 6 OCT 2023
Accepted 22 APR 2024

Author Contributions:

Conceptualization: Laura A. Stevens, Sarah B. Das, Mark D. Behn, Jeffrey J. McGuire, Ching-Yao Lai, Ian Joughin, Meredith Nettles
Data curation: Laura A. Stevens, Sarah B. Das, Mark D. Behn, Ian Joughin
Formal analysis: Laura A. Stevens, Ching-Yao Lai, Stacy Larochelle
Funding acquisition: Laura A. Stevens, Sarah B. Das, Mark D. Behn, Ching-Yao Lai, Ian Joughin, Meredith Nettles
Investigation: Laura A. Stevens, Sarah B. Das, Mark D. Behn, Ching-Yao Lai, Ian Joughin, Stacy Larochelle
Methodology: Laura A. Stevens, Sarah B. Das, Mark D. Behn, Jeffrey J. McGuire,

© 2024. The Authors.
This is an open access article under the terms of the Creative Commons Attribution License, which permits use, distribution and reproduction in any medium, provided the original work is properly cited.

1. Introduction

The inland migration of surface melt observed across the Greenland Ice Sheet over recent decades is unprecedented in the observational era, and controls on whether emerging surface meltwater can access the bed locally are not fully understood (Culberg et al., 2021; MacFerrin et al., 2019). Although observational evidence (Chudley et al., 2019; Das et al., 2008; Doyle et al., 2013; Stevens et al., 2015; Tedesco et al., 2013) and theoretical work (Alley et al., 2005; Krawczynski et al., 2009; van der Veen, 2007) support the ability of water stored in supraglacial lakes to hydro-fracture to the bed through thick ice, the likelihood of lake drainage via hydro-fracture at any particular location is controlled by the near-surface stress state rather than by water volume alone (Stevens et al., 2015). It has been hypothesized that an inland migration of surface melt that can access the bed could destabilize significant regions of the ice sheet (Alley et al., 2005; Leeson et al., 2015); however, it is currently unclear how vulnerable inland ice is to hydro-fracture. The vulnerability of the inland ice-sheet to increases in

21699011, 2024, 5, Downloaded from https://agupubs.onlinelibrary.wiley.com/doi/10.1029/2023JF007481 by Test, Wiley Online Library on [27/06/2024]. See the Terms and Conditions (https://onlinelibrary.wiley.com/terms-and-conditions) on Wiley Online Library for rules of use; OA articles are governed by the applicable Creative Commons License

Ching-Yao Lai, Ian Joughin, Stacy Larochelle
Project administration: Laura A. Stevens, Sarah B. Das, Mark D. Behn, Jeffrey J. McGuire, Ian Joughin, Meredith Nettles
Resources: Laura A. Stevens, Sarah B. Das, Mark D. Behn, Jeffrey J. McGuire, Ching-Yao Lai, Ian Joughin, Meredith Nettles
Software: Laura A. Stevens, Mark D. Behn, Jeffrey J. McGuire, Stacy Larochelle
Supervision: Laura A. Stevens, Sarah B. Das, Mark D. Behn, Jeffrey J. McGuire, Ian Joughin, Meredith Nettles
Validation: Laura A. Stevens, Ching-Yao Lai, Stacy Larochelle
Visualization: Laura A. Stevens
Writing – original draft: Laura A. Stevens
Writing – review & editing: Laura A. Stevens, Sarah B. Das, Mark D. Behn, Jeffrey J. McGuire, Ching-Yao Lai, Ian Joughin, Stacy Larochelle, Meredith Nettles

surface-meltwater-induced sliding depends, in part, on the ability of surface-to-bed meltwater pathways to develop in regions of nascent lake formation (Hoffman et al., 2018; Poinar et al., 2015).

One method for determining whether fractures can initiate and propagate to the ice-sheet bed beneath lakes is to calculate where ice-sheet tensile stresses and water pressures within fractures exceed the lithostatic stress and fracture toughness of ice (van der Veen, 1998, 2007; Weertman, 1973). Nearly all Greenland supraglacial lakes have sufficient water to keep a full-thickness fracture filled with water (Krawczynski et al., 2009). However, attempts to observe strain rates that could be used to estimate whether stresses within lake basins are sufficient to initiate fracture have proven unsuccessful on a regional scale, owing to insufficient temporal sampling and the low signal-to-noise ratio of satellite-based velocity products (Poinar & Andrews, 2021).

Christoffersen et al. (2018) have hypothesized that the inland migration of surface-to-bed pathways can occur via stress coupling between low- and high-elevation lake basins over very large distances (~80 km) during "cascading lake drainage" events, where "many lakes drain collectively in a chain reaction." They rely on a catalog of remotely sensed lake-drainage dates (Fitzpatrick et al., 2014), implicitly assuming that all lake drainages in the catalog occur by hydrofractures. However, the remotely sensed observations lack the spatio-temporal resolution required to determine whether the lake-drainage events in question occur via a basin overspill (e.g., Tedesco et al., 2013) or a hydro-fracture (e.g., Das et al., 2008). Other studies show that 72%–86% of lakes in southwest Greenland are observed to drain over durations that are too long (≥2 days) to occur via hydro-fracture (Fitzpatrick et al., 2014; Selmes et al., 2011).

Although drainage by overspill occurs when lake water height breaches the local lake-basin elevation (Tedesco et al., 2013), drainage by hydro-fracture requires a change in ice-sheet stress to initiate hydro-fracture and subsequent lake drainage (Stevens et al., 2015). Two leading mechanisms in which the drainage of one lake may promote or inhibit another lake to drain via hydro-fracture are: (a) ice-sheet deformation and basal slip directly associated with the initial lake drainage generates a change in ice-sheet stress within a different lake basin, and (b) hydraulic and bed-traction changes along the ice-sheet basal boundary, caused by evolving subglacial hydrologic conditions following the initial drainage, generate a change in ice-sheet stress within a different lake basin (Andrews et al., 2018; Christofferson et al., 2018; Hoffman et al., 2018; Poinar & Andrews, 2021). Both of these mechanisms act over elastic and viscous timescales of glacial-ice deformation (Lai et al., 2021; Pimentel & Flowers, 2011).

Here, we use a case study of adjacent lakes on the western margin of the Greenland Ice Sheet at an elevation of ~1,000 m above sea level to test the first mechanism. These lakes are known from previous in situ observations to drain via hydro-fracture close in time (Das et al., 2008; Stevens et al., 2015). We observationally constrain elastic ice-sheet stresses in the three neighboring lake basins to investigate the likelihood that stress coupling during the rapid drainage of a central lake could initiate the drainage of neighboring lakes via hydro-fracture. Ice-sheet deformation is observed using an array of global positioning system (GPS) stations that operated during 2011–2012 surrounding "North Lake" (Das et al., 2008) (Figure 1a). The three lakes we consider will be referred to as North Lake/L1A (68.72°N, 49.50°W; previously studied by Das et al. (2008), Stevens et al. (2015, 2016, 2018), and Lai et al. (2021)); L1B (68.70°N, 49.53°W); and L1C (68.75°N, 49.51°W) (Figures 1c–1f). North Lake (L1A) is the central lake, which fills and drains annually. The two neighboring lakes, L1B and L1C, drain together with L1A in some years but not in others. Using the GPS data, we calculate strain rates and derive estimates of stress change for the three lake basins during two rapid drainages of L1A. Previous in situ efforts have focused on the drainage dynamics of individual lakes (Chudley et al., 2019; Das et al., 2008; Doyle et al., 2013; Stevens et al., 2015), but our data provide measurements of sufficient spatial density (1–2 km) and extent (100 km^2) to evaluate drainage dynamics for our population of neighboring lakes, spaced 2–4 km apart. We consider our results for the 2011 and 2012 drainage events in the context of a 24-year record of drainage timing (Figure 1b), and analyze our findings together with idealized lake-drainage scenarios to provide a physical explanation for temporally clustered, hydro-fracture-driven drainages.

2. Data and Methods

2.1. GPS Data

An array of dual-frequency Trimble NetR9 GPS receivers (Trimble, Westminster, Colorado) (15 in 2011 and 16 in 2012) surrounding the three neighboring lake basins recorded two melt seasons of ice-sheet surface displacement,

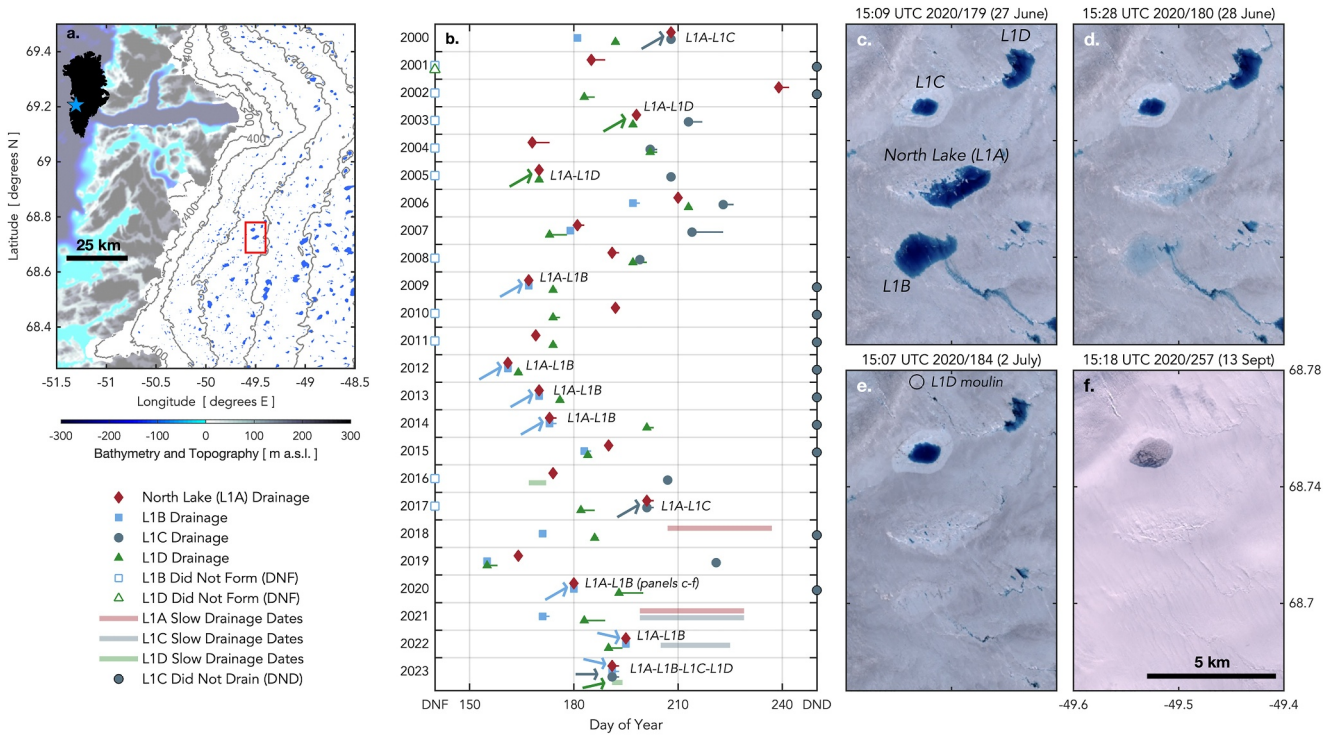

Figure 1. Neighboring supraglacial lakes on the Greenland Ice Sheet. (a) Supraglacial-lake maximum extents (blue areas on ice sheet) during 2000–2010 from Yang et al. (2015). Gray lines show ice-sheet surface elevation 200-m contours from BedMachine v3 (Morlighem et al., 2017). Red rectangle shows location of North Lake region shown in panels (c–f). (b) Timeseries of lake-drainage dates (symbols: see legend) and drainage-date uncertainties (thin horizontal bars) for L1A–D compiled from the Cooley and Christoffersen (2017) catalog from 2000 to 2015, and amended by GPS observations in 2006 and 2011–2013 (Das et al., 2008; Stevens et al., 2015) and review of Sentinel-1, Sentinel-2, Landsat-7, and Landsat-8 imagery from 2000 to 2023 (Table S2 in Supporting Information S1). Drainage co-occurrences within the error of drainage-date uncertainties are shown for L1A–L1B (blue arrows), L1A–L1C (gray arrows), and L1A–L1D (green arrows). (c)–(f) Sentinel-2 images showing L1A–D before, during, and after the drainage of L1A and L1B in late June, 2020. Final image shows the surface of L1C freezing over in mid-September, 2020.

including the rapid drainage of North Lake (L1A) on day 169 of 2011 (2011/169) and day 161 of 2012 (2012/161). In 2012, three additional GPS receivers were deployed up- and down-flow of the central array (Figure 2a). GPS data were processed as kinematic sites relative to the 30-s resolution Greenland GPS Network KAGA base station on bedrock ∼55 km away (Bevis et al., 2012) using the TRACK module (Chen, 1998) of the GAMIT/GLOBK (v. 10.4) software package (Herring et al., 2010). Formal uncertainties for horizontal position estimates are typically ∼0.02 m, for all stations and in both years (Stevens et al., 2015, 2016). The mean flow direction across the GPS array—calculated as the direction of horizontal velocities averaged over all stations in the two days prior to lake drainage—is 277° in 2011 (Figure S1a in Supporting Information S1) and 276° in 2012 (Figure 3a).

2.2. Strain Rates From GPS Surface-Position Estimates

To determine the effect of rapid lake drainage on ice-sheet surface strain rates at neighboring basins, we calculate horizontal strain rates $\dot{\varepsilon}$ between GPS stations from the horizontal components of surface-position estimates. We calculate horizontal strain rates both along and perpendicular to the ice-sheet flow direction because field observations indicate hydro-fractures can occur striking along or nearly orthogonal to the flow direction (Das et al., 2008; Doyle et al., 2013). After rotating the horizontal position estimates into the along- and across-flow directions (e.g., Figures 2b and 2c), we calculate the components of the horizontal strain rate, averaged over the distance between stations, in two dimensions according to Nye (1957):

$$\dot{\varepsilon} = \begin{bmatrix} \dfrac{\partial \dot{u}_x}{\partial x} & \dfrac{1}{2}\left(\dfrac{\partial \dot{u}_y}{\partial x} + \dfrac{\partial \dot{u}_x}{\partial y}\right) \\ \dfrac{1}{2}\left(\dfrac{\partial \dot{u}_y}{\partial x} + \dfrac{\partial \dot{u}_x}{\partial y}\right) & \dfrac{\partial \dot{u}_y}{\partial y} \end{bmatrix} = \begin{bmatrix} \dot{\varepsilon}_{xx} & \dot{\varepsilon}_{xy} \\ \dot{\varepsilon}_{yx} & \dot{\varepsilon}_{yy} \end{bmatrix}, \quad (1)$$

21699011, 2024, 5, Downloaded from https://agupubs.onlinelibrary.wiley.com/doi/10.1029/2023JF007481 by Test, Wiley Online Library on [27/06/2024]. See the Terms and Conditions (https://onlinelibrary.wiley.com/terms-and-conditions) on Wiley Online Library for rules of use; OA articles are governed by the applicable Creative Commons License

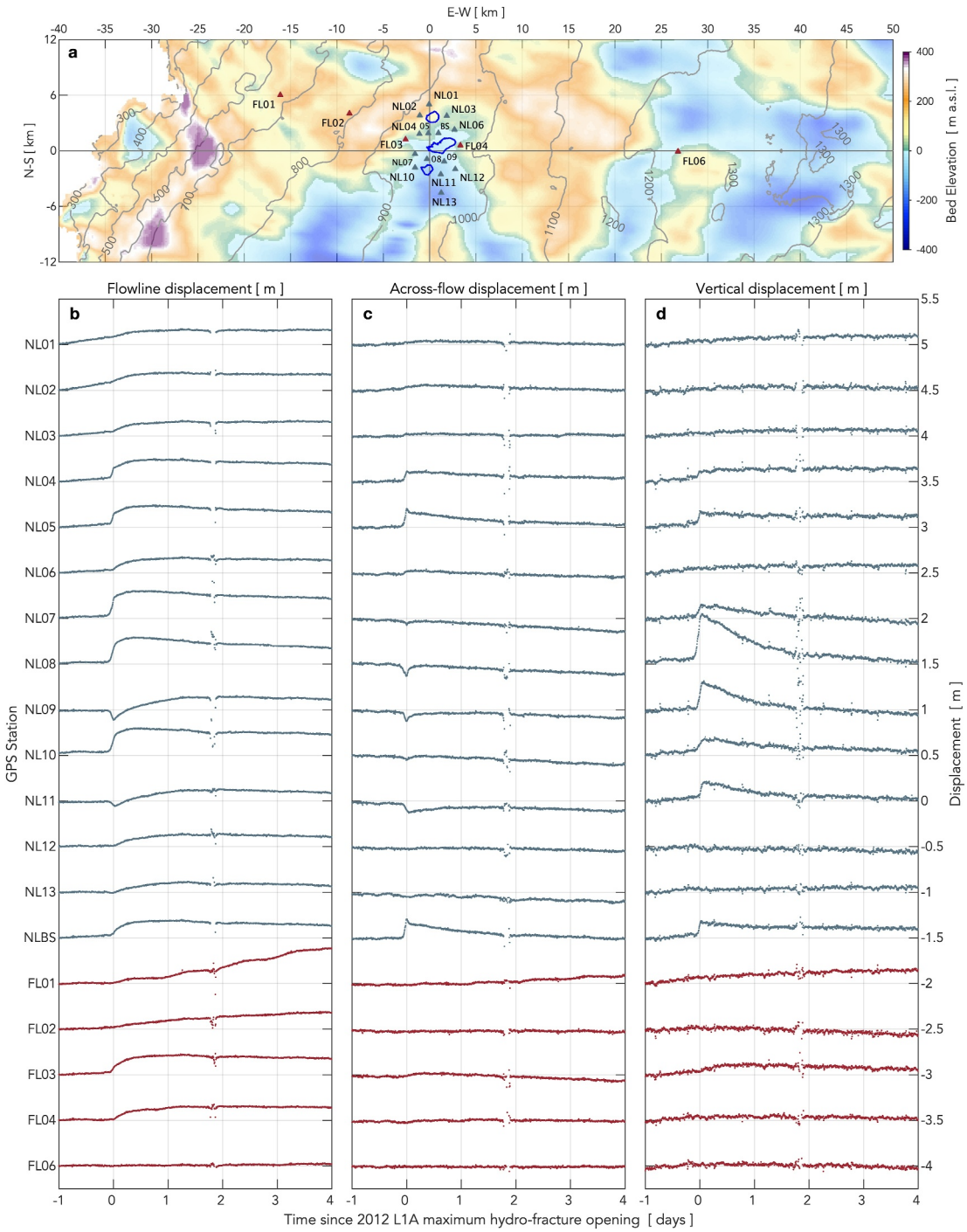

Figure 2. Flowline, across-flow, and vertical displacements of the GPS array during the 2012 L1A rapid drainage. (a) GPS station locations and ice-sheet (gray, 100-m contours) surface and (colormap) bed elevations from BedMachine v3 (Morlighem et al., 2017); coordinates are relative to a prominent moulin along the L1A hydro-fracture (Stevens et al., 2015), with the *x*-axis oriented east-west. Red triangles indicate flowline GPS stations (FL01–FL04, FL06); gray triangles indicate the main GPS array (NL01–NL13, NLBS). Lake outlines for L1A–C are shown in blue. (b) Flowline, (c) across-flow, and (d) vertical displacements for main array (gray) and flowline stations (red). Traces are offset by 0.5 m on the *y*-axis. Stations are ordered roughly north to south for the main array and down-to up-flow for the flowline array. Displacements more than 3σ from the mean are identified and removed, with the mean value determined using a moving-average filter 4 days in width as in Lai et al. (2021). A period of noisy data at all stations remains at day ∼1.8. A station named "FL05" was installed between FL04 and FL06; data from FL05 are not available on these days.

21699011, 2024, 5, Downloaded from https://agupubs.onlinelibrary.wiley.com/doi/10.1029/2023JF007481 by Test, Wiley Online Library on [27/06/2024]. See the Terms and Conditions (https://onlinelibrary.wiley.com/terms-and-conditions) on Wiley Online Library for rules of use; OA articles are governed by the applicable Creative Commons License

21699011, 2024, 5, Downloaded from https://agupubs.onlinelibrary.wiley.com/doi/10.1029/2023JF007481 by Test, Wiley Online Library on [27/06/2024]. See the Terms and Conditions (https://onlinelibrary.wiley.com/terms-and-conditions) on Wiley Online Library for rules of use; OA articles are governed by the applicable Creative Commons License

Where $\dot{u}_x$ and $\dot{u}_y$ are the horizontal components of velocity in the along- and across-flow directions, respectively; $\dot{\varepsilon}_{xx}$ is the strain rate in the along-flow direction; $\dot{\varepsilon}_{yy}$ is the strain rate in the across-flow direction; and, $\dot{\varepsilon}_{xy}$ is the horizontal shear strain rate. Components of $\dot{\varepsilon}$ between station pairs are calculated by differencing 20-min-resolution position and velocity estimates. The 20-min position estimates for each station are calculated by smoothing the 30-s positions (Figures 2b and 2c) with a centered boxcar filter 1-hr in width and then extracting positions every 20 min (Andrews et al., 2018). These 20-min positions are then used to calculate 20-min velocity estimates for each station using central differences. Errors in $\dot{\varepsilon}_{xx}$ and $\dot{\varepsilon}_{yy}$ can be estimated with arithmetic error propagation through Equation 1 yielding:

$$\delta\dot{\varepsilon}_{xx} = |\dot{\varepsilon}_{xx}|\sqrt{\frac{1}{\partial\dot{u}_x^2}\left(\delta x_2(T_{n+1})^2 + \delta x_2(T_{n-1})^2 + \delta x_1(T_{n+1})^2 + \delta x_1(T_{n-1})^2\right) + \frac{1}{\partial x^2}\left(\delta x_2(T_{n+1}) + \delta x_2(T_{n-1}) + \delta x_1(T_{n+1}) + \delta x_1(T_{n-1})\right)}, \tag{2}$$

$$\delta\dot{\varepsilon}_{yy} = |\dot{\varepsilon}_{yy}|\sqrt{\frac{1}{\partial\dot{u}_y^2}\left(\delta y_2(T_{n+1})^2 + \delta y_2(T_{n-1})^2 + \delta y_1(T_{n+1})^2 + \delta y_1(T_{n-1})^2\right) + \frac{1}{\partial y^2}\left(\delta y_2(T_{n+1}) + \delta y_2(T_{n-1}) + \delta y_1(T_{n+1}) + \delta y_1(T_{n-1})\right)}, \tag{3}$$

where x_1 is the position of the first GPS station, x_2 is the position of the second GPS station, T_{n+1} is the time of the position estimate 20 min ahead in time, and T_{n-1} is the time of the position estimate 20 min earlier in time. One-standard-deviation errors of the 30-s horizontal position estimates from TRACK, δx and δy, are consistently near 0.02 m. Strain-rate errors are on the order of 10^{-5} yr^{-1} (Figures S3 and S4 in Supporting Information S1).

During lake drainages, observations show changes in the direction of horizontal displacement over distances as short as 2–3 km (2–3 ice thicknesses) within the GPS array (Figure 2), indicating that strain rates can be variable over these short distances. Because the intersection of a crevasse and a lake is required for water from a lake to drive hydro-fracture (Krawczynski et al., 2009), we present strain rates for station pairs with inter-station baselines that cross a single lake. Strain rates for station pairs with inter-station baselines that bisect two or more lakes yield an averaged strain rate across those basins, and thus do not accurately resolve strain rates for individual lakes. An example of this strain-rate-averaging effect for inter-station baselines that bisect two lakes is provided in Figure S5 of Supporting Information S1.

2.3. Modeled Stresses From Network Inversion Filter (NIF) Deformation Estimates

To determine the effect of rapid lake drainage on ice-sheet stresses in neighboring basins, we (a) implement the NIF algorithm (Segall & Matthews, 1997) to estimate the space-time history of slip and opening along pre-defined planes within an isotropic, elastic half-space (Okada, 1985) that best reproduces GPS observations of ice-sheet surface deformation (Stevens et al., 2015), and (b) use these slip and opening estimates to forward model ice-sheet englacial stresses, which we evaluate at the ice-sheet surface (Stevens & Larochelle, 2024). Similar to the NIF implementation in Stevens et al. (2015), three deformation sources are included within the half-space: (a) hydro-fracture opening (due to water-driven fracture propagation through the ice sheet), (b) basal cavity opening (due to the rapid injection of meltwater at the ice-bed interface), and (c) extra basal slip above the background rate (due to enhanced basal lubrication) (Figure 3b–3d).

To estimate mode-I hydro-fracture opening, we define a vertical plane that strikes along the recurring L1A hydro-fracture scarp (Stevens et al., 2015). The vertical plane extends 1 km in length along dip, starting from a near-surface depth of 10^{-9} m within the half-space. The basal plane for estimating basal cavity opening (mode-I opening) and extra basal slip (dip-slip motion) is a sub-horizontal plane centered beneath L1A. In contrast to the NIF implementation in Stevens et al. (2015), here we increase the extent of the basal plane from 100 to 400 km^2 to ensure that the L1B and L1C basins are well within the extent of the basal plane (e.g., Figure 3e). The 400 km^2 basal plane is subdivided into 576 (24 × 24) subfaults to preserve the 0.83 km × 0.83 km size of subfault squares in Stevens et al. (2015). Although the extended basal plane presents an opportunity to interpret basal cavity opening and extra basal slip outside of the extent of the GPS array, we confine our analysis to stresses and lake basins within the footprint of the GPS array because we do not have observational constraints on ice-sheet displacements outside of this region. We choose to extend the NIF to only 1 day after the time of maximum L1A hydro-fracture opening because the assumption that linear elastic behavior is the dominant mode of ice-sheet

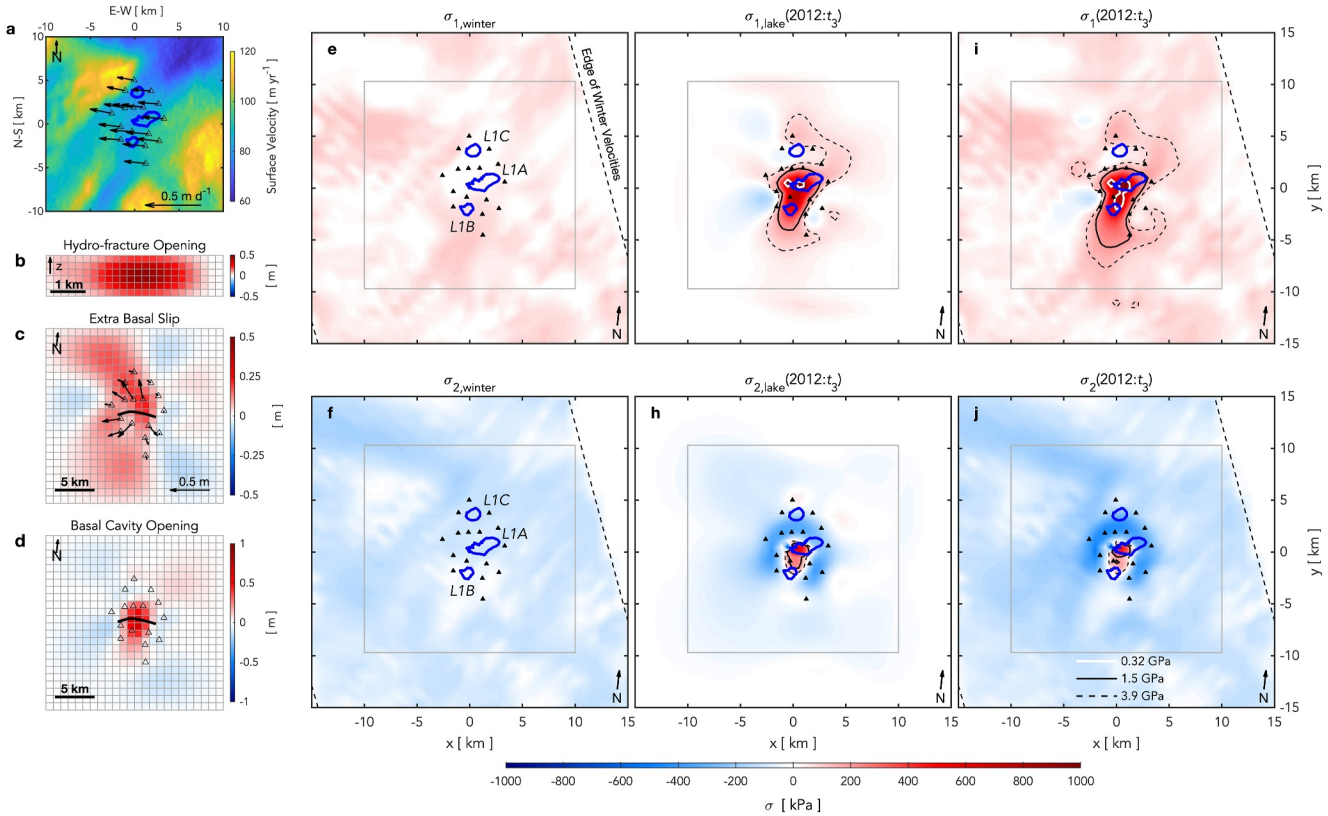

Figure 3. Forward modeling principal surface stresses from Network Inversion Filter (NIF) deformation estimates. (a) GPS network (triangles), lake outlines (blue), and 2009–2011 winter velocities derived from TerraSAR–X images (colormap) (Joughin et al., 2013), with the x-axis oriented east–west. GPS station velocities (black arrows) shown for the 2 days prior to the start of the lake drainage precursor (t_1). NIF-derived (b) hydro-fracture opening, (c) extra basal slip, and (d) basal cavity opening at the time of maximum L1A hydro-fracture opening (t_3) in 2012. L1A hydro-fracture scarp shown in black. The horizontal extent of the vertical hydro-fracture plane in panel (b) is the length of the hydro-fracture scarp in panels (c and d). On panel (c), black arrows show GPS observations of horizontal displacement from t_1 to t_3. (e) Maximum $\sigma_{1,\text{winter}}$ and (f) minimum $\sigma_{2,\text{winter}}$ horizontal principal surface stresses calculated from TerraSAR–X velocities in panel (a), with the x-axis oriented in the along-flow direction (277°). $\sigma_{1,2} > 0$ indicates tension. Gray square shows the extent of the NIF basal plane (panels c and d). (g) Maximum $\sigma_{1,\text{lake}}$ and (h) minimum $\sigma_{2,\text{lake}}$ horizontal principal stresses coincident with lake-drainage deformation in panels (b–d) for a shear modulus $\mu = 1.5$ GPa. Total (i) σ_1 and (j) σ_2 from winter velocity stresses (e and f) plus lake-drainage stresses (g and h) for a shear modulus $\mu = 1.5$ GPa. Panels (g–j) show 200-kPa contours in stress for $\mu = 0.32$ GPa (white line), $\mu = 1.5$ GPa (black line), and $\mu = 3.9$ GPa (dashed black line). There are no values >200 kPa in panels (e and f).

deformation is not justified for timescales longer than the Maxwell relaxation time τ of glacial ice (6–24 hr) (Krawczynski et al., 2009; van der Veen, 2007).

We use the NIF estimates of the space-time distribution of slip and opening along the pre-defined planes to forward model ice-sheet englacial (i.e., half-space) stresses during L1A rapid drainages. Using the Okada (1985) Green functions, we estimate x- and y-direction displacement-gradient components $\frac{\partial u_i}{\partial x_j}$ for 1,681 locations at 500-m spacing over a 400-km^2 region at the ice-sheet surface as a function of time t following

$$\frac{\partial u_i}{\partial x_j}(t)_{[k,1]} = G^{ij}_{[k,l]}\, s(t)_{[l,1]}, \tag{4}$$

where $u_i \in \{u_x, u_y, u_z\}$, $x_j \in \{x, y, z\}$, and $G^{ij}_{[k,l]}$ is the elastic Green function for each displacement-gradient component for locations k on the half-space surface due to slip (or opening) s on deformation-plane subfaults l comprising the hydro-fracture and basal planes. Free-surface boundary conditions at the half-space surface $(\varepsilon_{xz} = \varepsilon_{yz} = 0\,; \sigma_{xz} = \sigma_{yz} = \sigma_{zz} = 0)$ result in displacement-gradient components in the z-direction of:

21699011, 2024, 5, Downloaded from https://agupubs.onlinelibrary.wiley.com/doi/10.1029/2023JF007481 by Test, Wiley Online Library on [27/06/2024]. See the Terms and Conditions (https://onlinelibrary.wiley.com/terms-and-conditions) on Wiley Online Library for rules of use; OA articles are governed by the applicable Creative Commons License

$$\begin{cases} \dfrac{\partial u_x}{\partial z} = -\dfrac{\partial u_z}{\partial x} \\ \dfrac{\partial u_y}{\partial z} = -\dfrac{\partial u_z}{\partial y} \\ \dfrac{\partial u_z}{\partial z} = -\dfrac{\nu}{1-\nu}\left(\dfrac{\partial u_x}{\partial x} + \dfrac{\partial u_y}{\partial y}\right) \end{cases}, \tag{5}$$

where ν is the Poisson ratio. The strain tensor ε_{ij} is then computed from the displacement gradients as

$$\varepsilon_{ij} = \frac{1}{2}\left(\frac{\partial u_i}{\partial x_j} + \frac{\partial u_j}{\partial x_i}\right). \tag{6}$$

Strain components are calculated independently for the three deformation sources (i.e., hydro-fracture opening, basal cavity opening, and extra basal slip), and summed to obtain the total strain ε. The temporal resolution of $\varepsilon(t)$ is 2.5 min, equivalent to the temporal resolution of the GPS position timeseries used in the NIF by Stevens et al. (2015), which is calculated by smoothing 30-s positions with a centered boxcar filter 2.5-min in width and then extracting positions every 2.5 min (Stevens et al., 2015).

To evaluate whether stress conditions are favorable for crevasse initiation, half-space stresses are calculated following

$$\sigma(t) = C\varepsilon(t), \tag{7}$$

where σ is the six-component stress tensor and C is the fourth-order stiffness matrix of material properties for an isotropic linear elastic material. Equation 7 can be written as

$$\begin{bmatrix} \sigma_{xx} \\ \sigma_{yy} \\ \sigma_{zz} \\ \sigma_{yz} \\ \sigma_{xz} \\ \sigma_{xy} \end{bmatrix} = \begin{bmatrix} \lambda+2\mu & \lambda & \lambda & 0 & 0 & 0 \\ \lambda & \lambda+2\mu & \lambda & 0 & 0 & 0 \\ \lambda & \lambda & \lambda+2\mu & 0 & 0 & 0 \\ 0 & 0 & 0 & \mu & 0 & 0 \\ 0 & 0 & 0 & 0 & \mu & 0 \\ 0 & 0 & 0 & 0 & 0 & \mu \end{bmatrix} \begin{bmatrix} \varepsilon_{xx} \\ \varepsilon_{yy} \\ \varepsilon_{zz} \\ 2\varepsilon_{yz} \\ 2\varepsilon_{xz} \\ 2\varepsilon_{xy} \end{bmatrix}, \tag{8}$$

where λ and μ are the Lamé constants. The Lamé constant λ is calculated as $\lambda = 2\mu\nu/1-2\nu$, where μ is the shear modulus. For these constants, we use values suitable for glacial ice, including $\nu = 0.3$ and values of shear modulus μ of [0.32, 1.5, 3.9] GPa (Hobbs, 1974; Krawczynski et al., 2009; Vaughan, 1993). These choices lead to values λ = [0.48, 2.25, 5.85] GPa. Given the large uncertainty in the appropriate μ for glacial ice, we assume errors in σ fall within the range of stresses estimated when $\mu = 0.32$ GPa and $\mu = 3.9$ GPa (Krawczynski et al., 2009).

We present σ in terms of the maximum σ_1 (most tensile) and minimum σ_2 (most compressive) principal stresses in the horizontal plane following

$$\sigma_{1,2} = \frac{\sigma_{xx}+\sigma_{yy}}{2} \pm \sqrt{\left(\frac{\sigma_{xx}-\sigma_{yy}}{2}\right)^2 + {\sigma_{xy}}^2}, \tag{9}$$

where σ_{xx} is the normal stress in the along-flow direction, σ_{yy} is the normal stress in the across-flow direction, and σ_{xy} is the horizontal shear stress. We focus on principal stresses in the horizontal plane because we are concerned with stresses that promote the opening of vertical fractures. We use a sign convention such that $\sigma_{1,2} > 0$ indicates tension. The direction of maximum principal stress θ_1 is then given by $\tan 2\theta_1 = 2\sigma_{xy}/(\sigma_{xx}-\sigma_{yy})$, with the direction of minimum principal stress θ_2 being $\theta_1 \pm 90°$. Following the solid-earth community convention

21699011, 2024, 5, Downloaded from https://agupubs.onlinelibrary.wiley.com/doi/10.1029/2023JF007481 by Test, Wiley Online Library on [27/06/2024]. See the Terms and Conditions (https://onlinelibrary.wiley.com/terms-and-conditions) on Wiley Online Library for rules of use; OA articles are governed by the applicable Creative Commons License

21699011, 2024, 5, Downloaded from https://agupubs.onlinelibrary.wiley.com/doi/10.1029/2023JF007481 by Test, Wiley Online Library on [27/06/2024]. See the Terms and Conditions (https://onlinelibrary.wiley.com/terms-and-conditions) on Wiley Online Library for rules of use; OA articles are governed by the applicable Creative Commons License

(Hardebeck & Okada, 2018), principal stress orientations in map-view are shown by the direction of θ_2; mode-I fractures will open with a strike direction parallel to the plotted direction of maximum compression.

Though ice-sheet stresses in the hours prior to hydro-fracture opening are estimated to reach 100s of kPa across the hydro-fracture plane (Stevens et al., 2015), we consider elastic stress estimates generated by lake-drainage deformation in the context of lower-magnitude ice-sheet-surface viscous stresses driven by long-term patterns of ice-flow (Catania et al., 2008). Background, viscous ice-sheet surface stresses are calculated using Glen's flow law (Glen, 1955) to convert surface strain rates derived from 150-m resolution TerraSAR-X 2009–2011 winter velocity observations (Joughin et al., 2013) (Figure 3a) to longitudinal $\sigma_{xx,\text{winter}}$ and transverse $\sigma_{yy,\text{winter}}$ stresses according to Nye (1957) as presented in Cuffey and Paterson (2010):

$$\sigma_{xx,\text{winter}} = A^{-\frac{1}{n}} \dot{\varepsilon}_E^{[1-n]/n} \dot{\varepsilon}_{xx,\text{winter}} \tag{10}$$

and

$$\sigma_{yy,\text{winter}} = A^{-\frac{1}{n}} \dot{\varepsilon}_E^{[1-n]/n} \dot{\varepsilon}_{yy,\text{winter}}, \tag{11}$$

where A is the creep parameter, taken to be 3.5×10^{-25} s^{-1} Pa^{-3} (Budd & Jacka, 1989); n is the creep exponent, taken to be 3 (Cuffey & Paterson, 2010); and $\dot{\varepsilon}_E$ is the two-dimensional effective strain rate, given by

$$\dot{\varepsilon}_E^2 = \frac{1}{2}\left[\dot{\varepsilon}_{xx}^2 + \dot{\varepsilon}_{yy}^2\right] + \dot{\varepsilon}_{xy}^2. \tag{12}$$

Background viscous stresses are presented as maximum and minimum principal stresses following Equation 9.

Finally, to obtain an estimate of total ice-sheet stress during the lake-drainage events (i.e., $\sigma_{1,2}$; Figures 3i and 3j), we add background winter stresses (i.e., σ_{winter}; Figures 3e and 3f) to lake-drainage deformation stresses summed from each of the three NIF deformation sources (i.e., $\sigma_{\text{lake}} = \sigma_{\text{HF}} + \sigma_{\text{bedslip}} + \sigma_{\text{bedopen}}$, where "HF" is the hydro-fracture opening, "bedslip" is extra basal slip, and "bedopen" is basal cavity opening; Figures 3g and 3h). To describe the spatial and temporal variability in σ_1 explained by individual stress components, we calculate the correlation coefficient r of linear regressions between individual decomposed fields and σ_1 at every timepoint in the inversion. We take a yield stress for glacial ice σ_c of 200 kPa as a lower bound for the stress required to initiate surface crevassing (Vaughan, 1993). Recent work suggests this threshold could be as high as 1 MPa (Ultee et al., 2020), though much smaller values could be required if pre-existing surface cracks are present.

2.4. Idealized Deformation Simulations

To compare our findings from the ice-sheet location within the GPS array to other ice-sheet locations where lakes drain at present or could drain in future, we use the forward-modeling approach detailed in Section 2.3 to calculate surface stresses for idealized lake-drainage simulations over a range of ice-sheet thicknesses H and lake-drainage volumes V. To simulate different ice-sheet thicknesses, the depth of the basal plane within the elastic half-space is set to H. The 400 km^2 basal plane for the idealized simulations is subdivided into 1,600 (40 × 40) subfaults to achieve subfault squares 0.5 km × 0.5 km in size (Figures 4b and 4c). Similar to previous approaches (Dow et al., 2015; Hewitt et al., 2018; Tsai & Rice, 2010), we model the geometry occupied by the drained lake at the ice-bed interface as a fluid-filled radial blister (Chase et al., 2021; Lai et al., 2021) of volume V, which we implement in the forward-modeling framework as basal cavity opening (Figure 4b). Full details on our choices for implementing basal cavity opening in these idealized simulations are provided in Text S1 of Supporting Information S1.

Insights from field observations and laboratory experiments (Chase et al., 2021; Lai et al., 2021) show that blister radius does not evolve substantially after the majority of the lake volume is injected into the ice-bed interface. The region of the bed over which basal slip occurs, however, is related to the region of the bed where water from the blister permeates into the surrounding subglacial drainage system (Lai et al., 2021). The spatial extent of this region evolves in the days following drainage (Stevens et al., 2015), with bed topography and subglacial hydraulic gradients dictating the distribution of basal slip during this time (Dow et al., 2015; Doyle et al., 2013). These observations inform our idealized simulations of basal-plane slip distribution for the time period in which linear

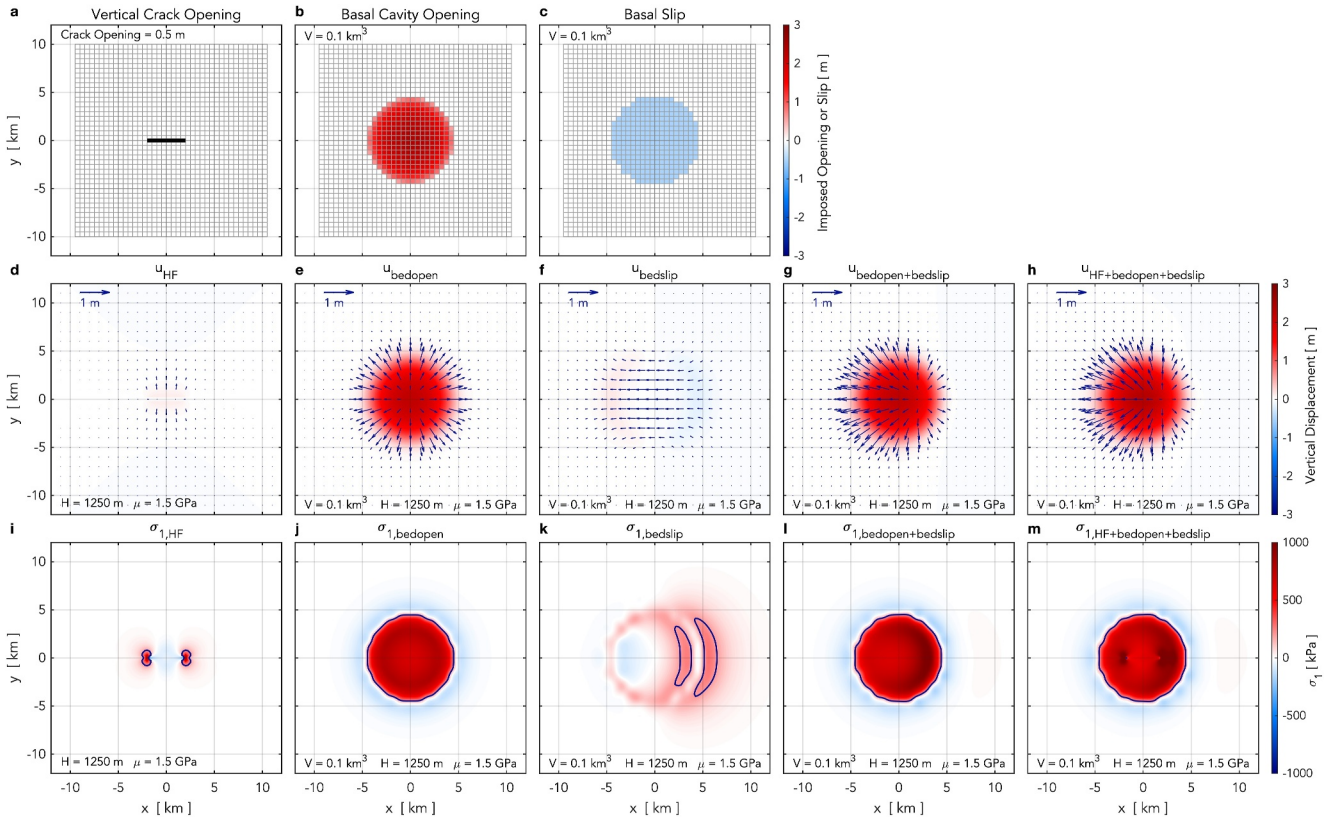

Figure 4. Forward modeling surface deformation and maximum principal surface stresses from idealized deformation distributions. (a) Plan-view location of 4-km-long vertical crack within the idealized Network Inversion Filter forward implementation. An opening of 0.5 m is imposed over the entire crack length and depth. Basal-plane subfaults are shown with gray squares. Idealized distributions of (b) basal cavity opening and (c) basal slip imposed on basal-plane subfaults for an idealized lake-drainage volume V of 0.1 km^3. Negative values of basal slip in panel c indicate 0.5 m of slip imposed in the along-flow direction (i.e., in the $-x$ direction). For a basal plane at a depth H of 1,250 m within the elastic half-space, surface displacements caused by (d) 0.5 m of opening along the vertical crack in panel (a); (e) the basal-cavity-opening distribution in panel (b); (f) the basal slip distribution in panel (c); (g) basal cavity opening and basal slip in panels (b and c); and, (h) the vertical crack opening, basal cavity opening, and basal slip in panels (a–c). Vectors show horizontal displacements; colormap shows vertical displacements. (i–m) Maximum horizontal principal stress coincident with deformation in panels (d–h), respectively, for a shear modulus μ of 1.5 GPa. The 200-kPa contour in stress is shown with a navy line.

elastic behavior is the dominant mode of ice-sheet deformation. We choose to mimic the slip distribution at the time of maximum hydro-fracture opening, when basal slip and basal cavity opening are roughly similar in horizontal extent (Figures 3c and 3d). Taking an upper-bound estimate for basal slip at the time of maximum hydro-fracture opening (Figure 3b), we impose 0.5 m of slip in the along-flow direction (i.e., in the –x direction) for all basal-plane subfaults within the radius of the fluid-filled blister (Figure 4c).

Figure 4 shows modeled displacements u (Figures 4d–4h) and maximum horizontal principal stresses σ_1 (Figures 4i–4m) at the elastic half-space surface for an idealized lake-drainage scenario with an H of 1,250 m, the largest-simulated V of 0.01 km^3, and a shear modulus μ of 1.5 GPa. Here, we also include an example of idealized, full-thickness hydro-fracture opening by imposing 0.5 m of opening over a 4-km-long, 1250-m-deep vertical plane striking east-west (i.e., along the x-axis; Figure 4a). This example illustrates that surface displacements generated by basal cavity opening and basal slip (Figures 4e and 4f) extend over a much wider region than surface displacements generated by hydro-fracture opening (Figure 4d). With the maximum NIF-estimated L1A vertical crack opening width in 2011 and 2012 being 0.14 and 0.46 m, respectively (Figure 3b; Figure S1b in Supporting Information S1), imposing 0.5 m of hydro-fracture opening over the entire vertical plane provides an upper-bound estimate for the influence of hydro-fracture opening on ice-sheet surface displacement and stress.

The idealized hydro-fracture opening example presents a common case for lake L1A where hydro-fracture opening occurs orthogonal to the ice-flow direction; however, hydro-fracture surface scarps are observed at many angles to the ice-flow direction in our study area (Figure 5a) and elsewhere (Chudley et al., 2019; Doyle

21699011, 2024, 5, Downloaded from https://agupubs.onlinelibrary.wiley.com/doi/10.1029/2023JF007481 by Test, Wiley Online Library on [27/06/2024]. See the Terms and Conditions (https://onlinelibrary.wiley.com/terms-and-conditions) on Wiley Online Library for rules of use; OA articles are governed by the applicable Creative Commons License

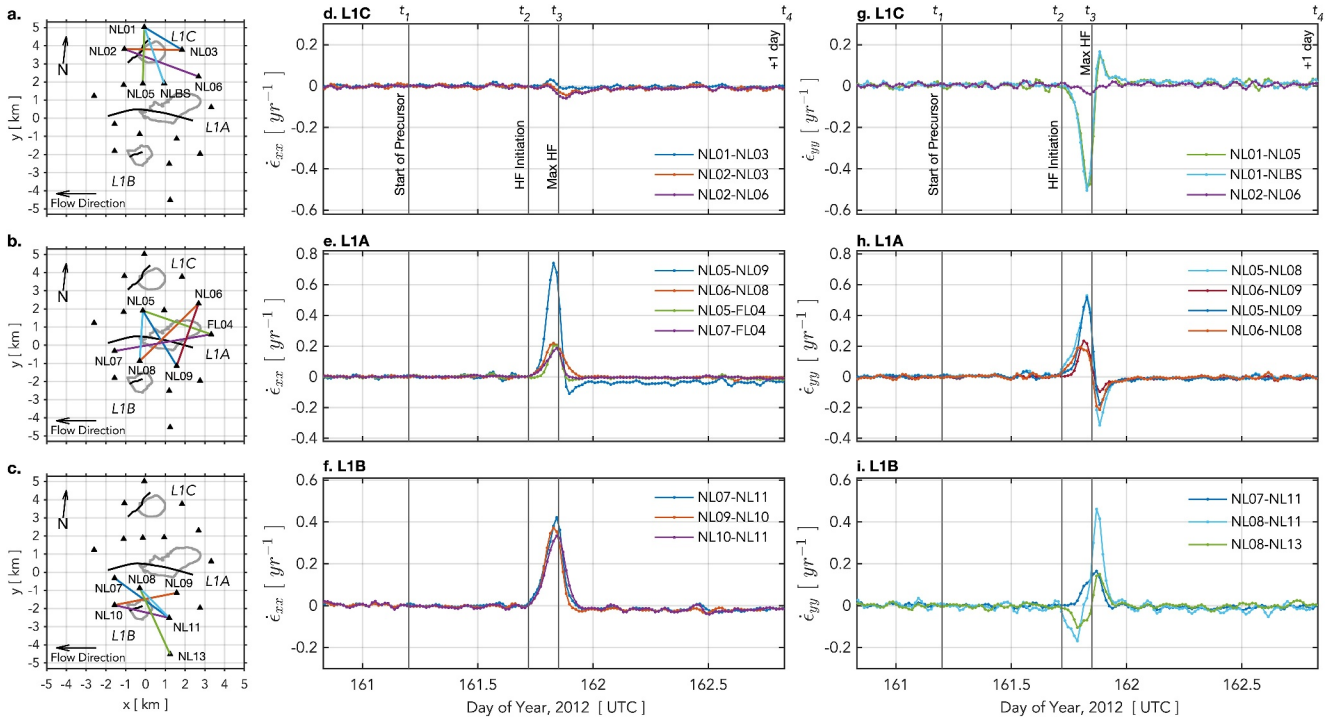

Figure 5. Neighboring lake basins experience contrasting observed horizontal strain rates during the 2012 rapid drainage of L1A. (a–c) GPS network (triangles), L1A–C lake margins (gray), and L1A–C hydro-fracture scarps (black). Solid lines show inter-station baselines used to calculate strain rates. (d–f) $\dot{\epsilon}_{xx}$ and (g–i) $\dot{\epsilon}_{yy}$ between select GPS station pairs. Dates are specified as day of year. Event timepoints $t_{1–4}$ are shown as vertical gray lines and along the top x-axis. The y-axis limits differ between panels. Strain-rate errors are shown in Figure S4 of Supporting Information S1.

et al., 2013). Given the diversity of observed hydro-fracture scarp strikes, and the fact that stresses from hydro-fracture opening decay quickly moving away from the crack (Figure 4i), we do not include a hydro-fracture opening term in the final presented idealized lake-drainage simulations. Instead, for the purposes of this study, we calculate and interpret surface stresses from (a) blister opening alone (Figure 4j), (b) basal slip alone (Figure 4k), and (c) the combination of these two deformation sources (Figure 4l), for 55 total combinations of H (500, 750, 1,000, 1,250, 1,500, 1,750, 2,000, 2,250, 2,500, 2,750, and 3,000 m) and V (0.001, 0.005, 0.01, 0.05, and 0.1 km^3) that span the relevant physical scales of supraglacial lake drainage through ice sheets.

2.5. Timeseries of Lake-Drainage Dates

To put our 2011 and 2012 GPS observations into a longer-term context, we compiled lake onset and drainage dates during 2000–2023 by reviewing satellite imagery and an existing catalog of lake-drainage dates that covers our study region (Cooley & Christoffersen, 2017). Cooley and Christoffersen (2017) used automated-image analysis to identify lake-drainage timing over a wide area of the western margin, producing a catalog of lake onset and drainage dates from 2000 to 2015 (Table S1 in Supporting Information S1). For this study, we focus on the ice-sheet footprint of lakes L1A–D (Figure 1c) from 2000 to 2023. In some years, the Cooley and Christoffersen (2017) catalog does not identify lake onset or drainage dates for L1A–D, though these lakes are known to have formed and drained from previously published studies (Stevens et al., 2015, 2016) using GPS observations and satellite imagery (Table S2 in Supporting Information S1). This inconsistency prompted us to review all available Landsat and Sentinel imagery from 2000 to 2023 to (a) rectify discrepancies between lake onset and drainage dates published in the Cooley and Christoffersen (2017) catalog and available imagery, and (b) extend the drainage-date record for these lakes through 2023 (Figure 1b; Table S2 in Supporting Information S1). Our imagery review suggests that, although Cooley and Christoffersen (2017) report a lake onset and drainage date in all years from 2000 to 2015 for L1C (Table S1 in Supporting Information S1), in roughly half of the years L1C does not drain at the end of the melt season, but rather the surface of L1C freezes over. Our catalog thus also differs from the Cooley and Christoffersen (2017) catalog because of our manual identification of years in which L1C freezes over at the end of the melt season, rather than draining, and is thus already present at the beginning of

21699011, 2024, 5, Downloaded from https://agupubs.onlinelibrary.wiley.com/doi/10.1029/2023JF007481 by Test, Wiley Online Library on [27/06/2024]. See the Terms and Conditions (https://onlinelibrary.wiley.com/terms-and-conditions) on Wiley Online Library for rules of use; OA articles are governed by the applicable Creative Commons License

21699011, 2024, 5, Downloaded from https://agupubs.onlinelibrary.wiley.com/doi/10.1029/2023JF007481 by Test, Wiley Online Library on [27/06/2024]. See the Terms and Conditions (https://onlinelibrary.wiley.com/terms-and-conditions) on Wiley Online Library for rules of use; OA articles are governed by the applicable Creative Commons License

the subsequent melt season. Where GPS data are available to constrain lake-drainage dates, we set the error in drainage date to zero days (Table S2 in Supporting Information S1).

3. Drainage Behavior Within the Study Area

North Lake (L1A), the central lake of the study cluster, has consistently formed and drained once per melt season from 2000 to 2023, as shown by GPS data (Das et al., 2008; Lai et al., 2021; Stevens et al., 2015, 2016) and satellite imagery (Cooley & Christoffersen, 2017) (Figure 1b). Drainage dynamics of North Lake were first studied by Das et al. (2008), who observed a drainage in 2006 to occur in <2 hr, via water-driven fracture propagation to the ice-sheet bed through 980 m of ice. A later study by Stevens et al. (2015) observed that hydro-fracture-driven drainages of North Lake in 2011, 2012, and 2013 were preceded by ice-sheet uplift and/or enhanced basal slip in the hours leading to hydro-fracture initiation. Ice-sheet deformation during these lake-drainage precursors generated tensile stresses of sufficient magnitude normal to a recurring fracture plane within the North Lake basin to temporarily overcome background compressive stresses and promote hydro-fracture beneath the lake (Stevens et al., 2015). The precursory ice-sheet uplift and enhanced basal slip were hypothesized to be caused by injection of water to the ice-sheet bed via neighboring moulins or hydro-fractures (Stevens et al., 2015). Following North Lake rapid drainages, water-filled blisters at the ice-bed interface maintain uplift for durations of 1–10 days, with the timescale of uplift relaxation driven by the transmissivity of the surrounding subglacial drainage system (Lai et al., 2021).

Lakes L1B, L1C, and L1D are located ∼2.0 km to the south, ∼3.5 km to the north, and ∼6.0 km to the northeast of North Lake (L1A), respectively (Figure 1c). The lake to the south, L1B, formed in 14 out of 24 years from 2000 to 2023 (Figure 1b). In the years that L1B did not form, the same supraglacial-stream network feeding the basin from the southeast that is present in all years re-activated one or more moulins within the lake basin without leading to lake formation. L1B was observed to drain rapidly within hours of L1A in 2012 and 2013 when GPS data were available (Table S2 in Supporting Information S1) (Stevens et al., 2015). In the 14 years that L1B formed during 2000–2023, L1B drained synchronously with L1A (i.e., within the 2–3-day temporal uncertainty of remotely sensed drainage dates) in exactly half of these years (Figure 1b; Table S2 in Supporting Information S1). The lake to the north, L1C, is present annually and, in roughly half of the years from 2000 to 2023, remnant lake ice from the previous winter persisted throughout the following melt season, indicating that the lake froze over without draining at the end of the previous melt season (Figure 1b). During the study period, L1C drained synchronously with L1A in 12.5% of years (Figure 1b; Table S2 in Supporting Information S1). In 2023, lakes L1A, L1B, and L1C are observed to drain between images taken three days apart, alongside an overspill drainage of lake L1D; this is the only quadruple-drainage event observed over the 24-year timeseries (Figure 1b; Table S2 in Supporting Information S1).

Surface traces of kilometer-scale fractures exist within L1A, L1B, and L1C basins in years of drainages, indicating that all three lakes do, at times, drain rapidly via hydro-fracture. The main L1A hydro-fracture scarp has an average strike of 281° (WNW), as digitized from a WorldView image taken on day 202 of 2011 (2011/202) (Stevens et al., 2015). A fracture has existed in this lake in roughly the same orientation since at least 2006 (Das et al., 2008). The L1B hydro-fracture scarp in the same 2011/202 image has an average strike of 248° (WSW). An empty L1C basin is not observable during the 7-year period when L1C does not drain from 2009 to 2015. We digitized an L1C hydro-fracture scarp with an average strike of 230° (SW) from a Sentinel-2 image in which a scarp is clearly visible on 2019/224.

4. Results

The 2011 and 2012 North Lake (L1A) drainages via hydro-fracture produce elastic stress changes in the L1B and L1C basins that differ, with L1B experiencing tensional stresses and L1C experiencing compressional stresses when L1A drains via hydro-fracture. For the two L1A drainage events, we present observed strain rates from GPS surface-position estimates (Section 4.1) and modeled elastic stresses using NIF deformation estimates (Section 4.2). In our analysis, we refer to four timepoints during the drainage events, as previously identified by Stevens et al. (2015): t_1, the start of the L1A drainage precursor; t_2, L1A hydro-fracture initiation; t_3, maximum L1A hydro-fracture opening; and t_4, one day following maximum L1A hydro-fracture opening. Our ice-sheet surface strain-rate observations and modeled stresses guide an idealized set of forward-modeling simulations of surface stresses over a range of lake-drainage volumes and ice-sheet thicknesses (Section 4.3).

21699011, 2024, 5, Downloaded from https://agupubs.onlinelibrary.wiley.com/doi/10.1029/2023JF007481 by Test, Wiley Online Library on [27/06/2024]. See the Terms and Conditions (https://onlinelibrary.wiley.com/terms-and-conditions) on Wiley Online Library for rules of use; OA articles are governed by the applicable Creative Commons License

4.1. Observed Strain Rates From GPS Surface-Position Estimates

During the two drainage events, short-lived horizontal strain-rate excursions in the two neighboring lake basins coincide with the drainage of L1A. Depending on the sign of the excursion, we interpret these strain-rate excursions as either promoting or inhibiting tensile crack opening compared to background strain rates observed prior to drainage events. The 2011 L1A drainage occurred over ∼3 hr on 2011/169 (Figure S2 in Supporting Information S1). In the days prior to drainage, longitudinal $\dot{\varepsilon}_{xx}$ (Figures S2d–S2f in Supporting Information S1) and across-flow $\dot{\varepsilon}_{yy}$ (Figures S2g–S2i in Supporting Information S1) strain rates are low ($<|0.05|\ \mathrm{yr}^{-1}$) for all lake basins. At L1A hydro-fracture initiation (t_2), L1A basin $\dot{\varepsilon}_{xx}$ and $\dot{\varepsilon}_{yy}$ are positive (extensional) and increase to 7 times the background rate (Figure S2e and S2h in Supporting Information S1), well above estimated error levels (Figures S3e and S3h in Supporting Information S1), by the time of maximum L1A hydro-fracture opening (t_3). L1A $\dot{\varepsilon}_{xx}$ are $>0.10\ \mathrm{yr}^{-1}$ for 2.7 hr. Because the L1A hydro-fracture scarp strikes 4° clockwise of the flow direction in 2011 (Figure S2a in Supporting Information S1), we expect to see the clearest signature of crack opening and closing in $\dot{\varepsilon}_{yy}$ (Figure S2h in Supporting Information S1). The closing signature of the L1A hydro-fracture is seen in negative (compressional) $\dot{\varepsilon}_{yy}$ immediately following the time of maximum L1A hydro-fracture opening (t_3; Figure S2h in Supporting Information S1). L1A basin strain rates return to background values ($<|0.05|\ \mathrm{yr}^{-1}$) within a few hours after maximum opening and remain low during the following days.

From t_2 to t_3, GPS station pairs across L1C show neutral $\dot{\varepsilon}_{xx}$ and compressional $\dot{\varepsilon}_{yy}$ (Figures S2d and S2g in Supporting Information S1). This strain-rate pattern indicates that the L1C basin is in a state of greater compression during the 2011 L1A drainage compared to pre-drainage strain rates. With the L1C hydro-fracture scarp striking 230° (ice-flow direction is 277°), either $\dot{\varepsilon}_{xx}$ or $\dot{\varepsilon}_{yy}$ would need to be extensional to promote opening of the fracture. By contrast, in the L1B basin from t_2 to t_3, positive values of $\dot{\varepsilon}_{xx}$ are observed (Figure S2f in Supporting Information S1), with L1B $\dot{\varepsilon}_{xx} > 0.10\ \mathrm{yr}^{-1}$ for 3.6 hr (Figure S2f in Supporting Information S1). In $\dot{\varepsilon}_{yy}$ for L1B, a signature opposite that of the L1A hydro-fracture crack opening-and-closing sequence is observed (Figure S2i in Supporting Information S1). These observations indicate that, during the 2011 L1A drainage, strain rates are extensional in the L1B basin.

Similar inter-basin strain-rate relationships were observed during the 2012 L1A drainage (Figure 5). This L1A drainage occurred over a ∼5-hr period on 2012/161. L1A basin $\dot{\varepsilon}_{xx}$ and $\dot{\varepsilon}_{yy}$ are elevated above pre-event strain rates from t_2 to t_3 (Figures 5e and 5h), well above estimated error levels (Figures S4e and S4h in Supporting Information S1). L1A basin $\dot{\varepsilon}_{xx}$ are $>0.10\ \mathrm{yr}^{-1}$ for 2.3 hr (Figure 5e). Simultaneously, neutral $\dot{\varepsilon}_{xx}$ (Figure 5d) and negative $\dot{\varepsilon}_{yy}$ (Figure 5g) are observed in the L1C basin, and positive $\dot{\varepsilon}_{xx}$ are observed in the L1B basin (Figure 5f), with L1B $\dot{\varepsilon}_{xx} > 0.10\ \mathrm{yr}^{-1}$ for 2.6 hr (Figure 5f).

4.2. Modeled Surface Stress and Stress Orientation Using NIF Deformation Estimates

Similar to NIF-derived deformation estimates at the time of maximum L1A hydro-fracture opening (t_3) in Stevens et al. (2015), basal cavity opening at t_3 in both the 2011 L1A drainage (Figure S1d in Supporting Information S1) and 2012 L1A drainage (Figure 3d) is observed in the central and southern regions of the array, with extra basal slip observed for most stations on the western (down-flow) side of the array (Figure 3c; Figure S1c in Supporting Information S1). Compared to Stevens et al. (2015), the extended size of the basal plane allows for extra basal slip and basal cavity opening estimates beyond the extent of the GPS array, which are not well constrained but are small in comparison to deformation estimates within the array. As described in Section 2.3, NIF-derived deformation estimates are used to model the lake-drainage-induced stresses σ_{lake} shown in Figures 3g and 3h and Figures S1g and S1h in Supporting Information S1. Background viscous stresses σ_{winter} (Figures 3e and 3f; Figures S1e and S1f in Supporting Information S1) are added to the lake-drainage-induced stresses σ_{lake} (Figures 3g and 3h; Figures S1g and S1h in Supporting Information S1) to obtain an estimate for total stress $\sigma_{1,2}$ (Figures 3i and 3j; Figures S1i and S1j in Supporting Information S1) during the lake-drainage events.

Time-series decompositions of spatially varying maximum principal stresses σ_1 ($\sigma_1 = \sigma_{1,\mathrm{winter}} + \sigma_{1,\mathrm{HF}} + \sigma_{1,\mathrm{bedopen}} + \sigma_{1,\mathrm{bedslip}}$) during the 2011 and 2012 L1A drainages show regions of both tension and compression in the three lake basins (Figure 6). Compared to $\sigma_{1,\mathrm{winter}}$ values, which are on the order of 0–100 kPa (Figure 6a), deformation due to the L1A drainage results in regions of highly tensile principal stresses over the L1A and L1B basins (i.e., where $\sigma_1 > \sigma_C$) that are not radially symmetric (Figures 6e and 6m). By contrast, σ_1 in the L1C basin is at most −100 kPa in 2011 (Figure 6i) and at most +100 kPa in 2012 (Figure 6q), indicating that the surface

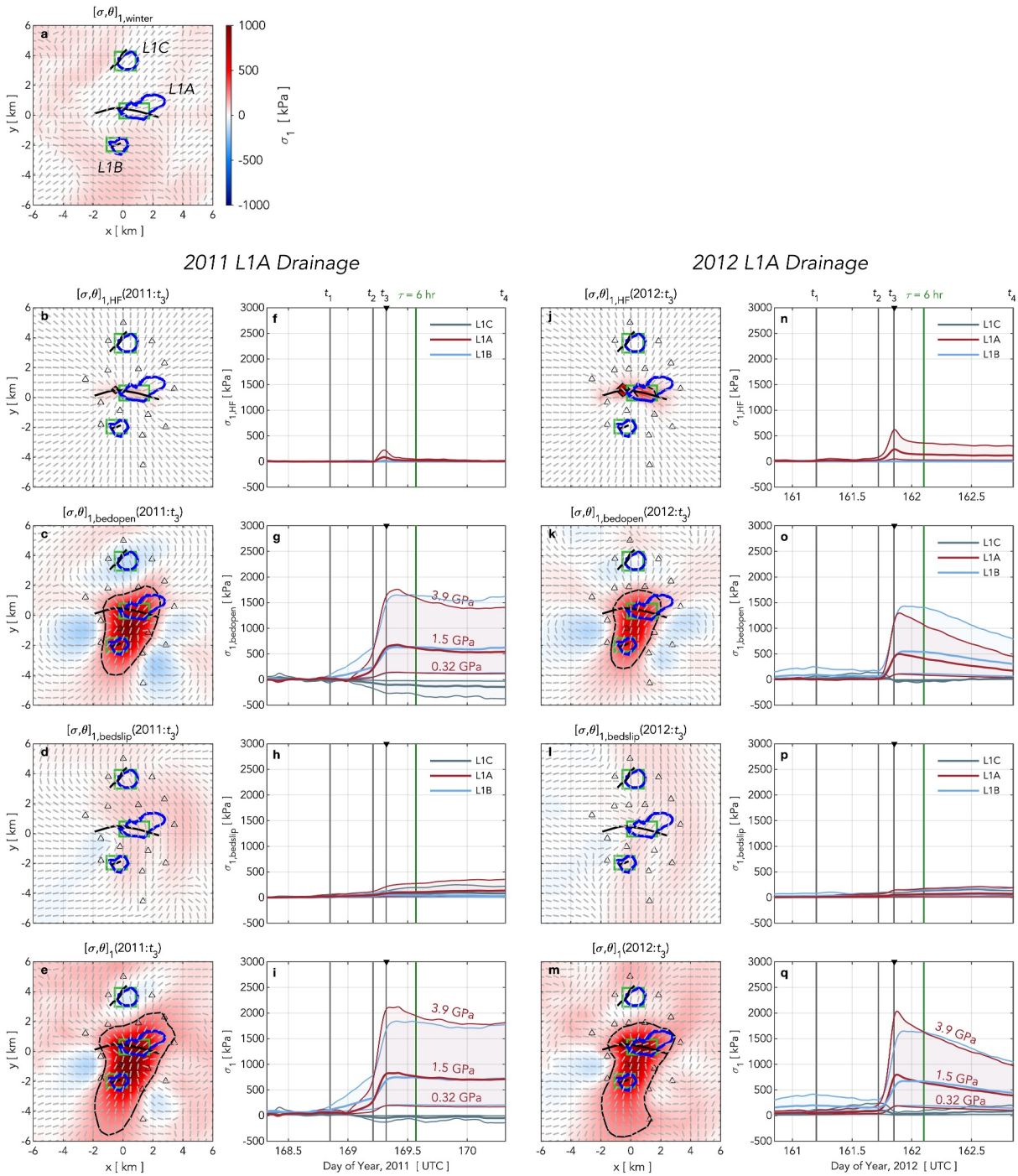

Figure 6. Modeled maximum principal stress during the 2011 and 2012 L1A drainages. (a) (gray bars) Orientation of $\theta_{1,\text{winter}}$ and (colormap) $\sigma_{1,\text{winter}}$ for $\mu = 1.5$ GPa. Gray bars are plotted for the orientation of the maximum horizontal compressive stress, such that tensile stress across a hydro-fracture scarp (thick black lines) plots with the bars parallel to the hydro-fracture scarp. (black triangles) GPS network and (blue) lake outlines are shown. (b)–(e) Equivalent to panel (a), but for (b) $[\sigma, \theta]_{1,\text{HF}}$, (c) $[\sigma, \theta]_{1,\text{bedopen}}$, (d) $[\sigma, \theta]_{1,\text{bedslip}}$, and (e) $[\sigma, \theta]_1$ at maximum L1A hydro-fracture opening (t_3) during the 2011 L1A drainage. Black contours show 200-kPa contour in stress. (f)–(j) Timeseries of area-averaged principal stress for each lake basin (green boxed areas in left-column panels). Event timepoints t_{1-4} and the approximate lower bound of 6-hr for the Maxwell time τ for glacial ice are shown as vertical lines and along the top x-axis. Thick center horizontal line shows area-averaged stress for $\mu = 1.5$ GPa. Outer lines show average stress for $\mu = 0.32$ GPa and $\mu = 3.9$ GPa, with the 3.9 GPa estimate always the furthest line from the x-axis. (k–t) Equivalent to panels (a–j) but for the 2012 L1A drainage. To be viewed alongside Movies S1 and S2.

21699011, 2024, 5, Downloaded from https://agupubs.onlinelibrary.wiley.com/doi/10.1029/2023JF007481 by Test, Wiley Online Library on [27/06/2024]. See the Terms and Conditions (https://onlinelibrary.wiley.com/terms-and-conditions) on Wiley Online Library for rules of use; OA articles are governed by the applicable Creative Commons License

21699011, 2024, 5, Downloaded from https://agupubs.onlinelibrary.wiley.com/doi/10.1029/2023JF007481 by Test, Wiley Online Library on [27/06/2024]. See the Terms and Conditions (https://onlinelibrary.wiley.com/terms-and-conditions) on Wiley Online Library for rules of use; OA articles are governed by the applicable Creative Commons License

stresses associated with L1A drainages are compressional to weakly tensile within the L1C basin. One day after maximum L1A hydro-fracture opening in 2011 and 2012, regions with $\sigma_1 > \sigma_C$ increase in spatial extent (Movies S1 and S2). These regions intersect the L1C margin in 2012 but not in 2011, and L1C persists through both the 2011 and 2012 melt seasons without draining (Figure 1b). The magnitude of σ_1 varies with the assumed value of μ, but the sense of the stress perturbation (i.e., positive or negative) is not sensitive to μ (Figures 3i and 6; Figure S1i in Supporting Information S1).

The decomposed stress field shows that stress contributions from hydro-fracture opening $\sigma_{1,\mathrm{HF}}$ are spatially localized to within 1 km of the L1A hydro-fracture plane (Figures 6b and 6j) and occur in time from t_2 onwards (Figures 6f and 6n). Stress contributions from extra basal slip $\sigma_{1,\mathrm{bedslip}}$ are low (−50 to +100 kPa) from t_1 to t_3 in 2011 and 2012 (Figures 6h and 6p), and are on the order of $\sigma_{1,\mathrm{winter}}$ (Figure 6a). Contributions from $\sigma_{1,\mathrm{bedslip}}$ grow gradually from t_3 to t_4 (Figures 6h and 6p) due to expansion of extra basal slip across the array. Stress from basal cavity opening $\sigma_{1,\mathrm{bedopen}}$ is the main contributor to total stress (σ_1) after t_2 (Figures 6c and 6k).

The spatial and temporal variability in σ_1 explained by individual stress components is formally described by the correlation coefficient r of linear regressions between individual decomposed fields and σ_1 (Figure 7) for stress values estimated within the $x \leq |6|$ km and $y \leq |6|$ km region plotted in Figure 6. For both drainages, the correlation coefficient r [$\sigma_{1,\mathrm{winter}}$, σ_1] decreases prior to and during the precursor (from t_1 to t_2; Figure 7) as deformation due to the lake drainage occurs on the basal and hydro-fracture planes. From t_2 onward, variability in σ_1 is increasingly explained by $\sigma_{1,\mathrm{bedopen}}$, with r [$\sigma_{1,\mathrm{bedopen}}$, σ_1] attaining maximum values of 0.98 (2011) and 0.94 (2012) in the hours following t_3 (Figure 7). Contributions to variability in σ_1 from $\sigma_{1,\mathrm{bedslip}}$ and $\sigma_{1,\mathrm{HF}}$ are generally lower than contributions from $\sigma_{1,\mathrm{bedopen}}$, although we observe that, in 2012, r [$\sigma_{1,\mathrm{HF}}$, σ_1] increases during the time of hydro-fracture opening from t_2 to t_3 (Figure 7). These regressions confirm that regions of highly tensile σ_1 track the extent of basal cavity opening (Figures 6c and 6k), which is dominantly expressed in the GPS data as ice-sheet surface uplift (Stevens et al., 2015; Tsai & Rice, 2010).

GPS stations along the northern and inland up-flow edges of the network (i.e., NL01–NL03, NL06, FL03, NL12, and NL13) show little to no uplift during the drainage events (Figures 2a and 2d), and σ_1 is consequently low in this area of the network (Figures 6e and 6m). Although we do not have dense GPS observations of ice-sheet deformation up- or down-flow of the central array, the stations located up- and down-flow of the L1A origin (FL06, at ∼26 km up-flow, and FL01 and FL02 at ∼9 km and ∼16 km down-flow) during the 2012 L1A drainage show no step-changes in along-flow, across-flow, or vertical displacements that are recorded by the central-array stations (i.e., NL04, NL05, NL07–NL10, and NLBS) (Figure 2).

During both L1A drainages, the orientation of maximum principal stress θ_1 within all three basins rotates >10° from estimated winter orientations (Figure S6 in Supporting Information S1). In the 2011 L1A drainage, L1B θ_1 rotates 111° clockwise from the basin's winter θ_1 by the time of maximum L1A hydro-fracture opening (t_3), while the L1A and L1C basins show counterclockwise rotations of 32° and 52°, respectively, over this same time period (Figures S6b and S6d in Supporting Information S1). Both L1A and L1B $\sigma_{1,2}$ are tensile at this time (Figures S1i and S1j in Supporting Information S1), such that the sign and orientation of $\sigma_{1,2}$ would promote fracture opening in roughly the direction of the mapped L1A and L1B hydro-fracture scarps. By contrast, in L1C, the $\sigma_{1,2}$ values at t_3 are compressive (Figures S1i and S1j in Supporting Information S1); this principal stress value and orientation would place the L1C hydro-fracture plane in compression. In the 2012 L1A drainage, L1A θ_1 rotates 5° counterclockwise from the basin's winter θ_1 by t_3, with L1B and L1C basins showing counterclockwise rotations of 76° and 25°, respectively (Figures S6c and S6e in Supporting Information S1). The sign and orientation of $\sigma_{1,2}$ in 2012 (Figures 3i and 3j) would promote fracture opening of L1A and L1B hydro-fracture planes and place the L1C hydro-fracture plane weakly in tension.

4.3. Modeled Surface Stress From Idealized Simulations

To investigate stress-coupling distances outside of the ice-sheet setting of our GPS array, we analyze our findings from the two L1A drainages alongside idealized lake-drainage simulations for a range of ice-sheet thicknesses H and lake-drainage volumes V given a shear modulus μ of 1.5 GPa (Figure 8). Stresses from equivalent idealized simulations where $\mu = 0.32$ GPa and $\mu = 3.9$ GPa are shown in Figures S7 and S8 in Supporting Information S1. For most of the tested parameter range, contributions to σ_1 from basal cavity opening are approximately four times larger than the contribution from basal slip. Pre-drainage-event ice-sheet surface stresses are taken to be zero in the idealized simulations, such that modeled values of $\sigma_{1,\mathrm{bedopen+bedslip}}$ from idealized lake-drainage simulations

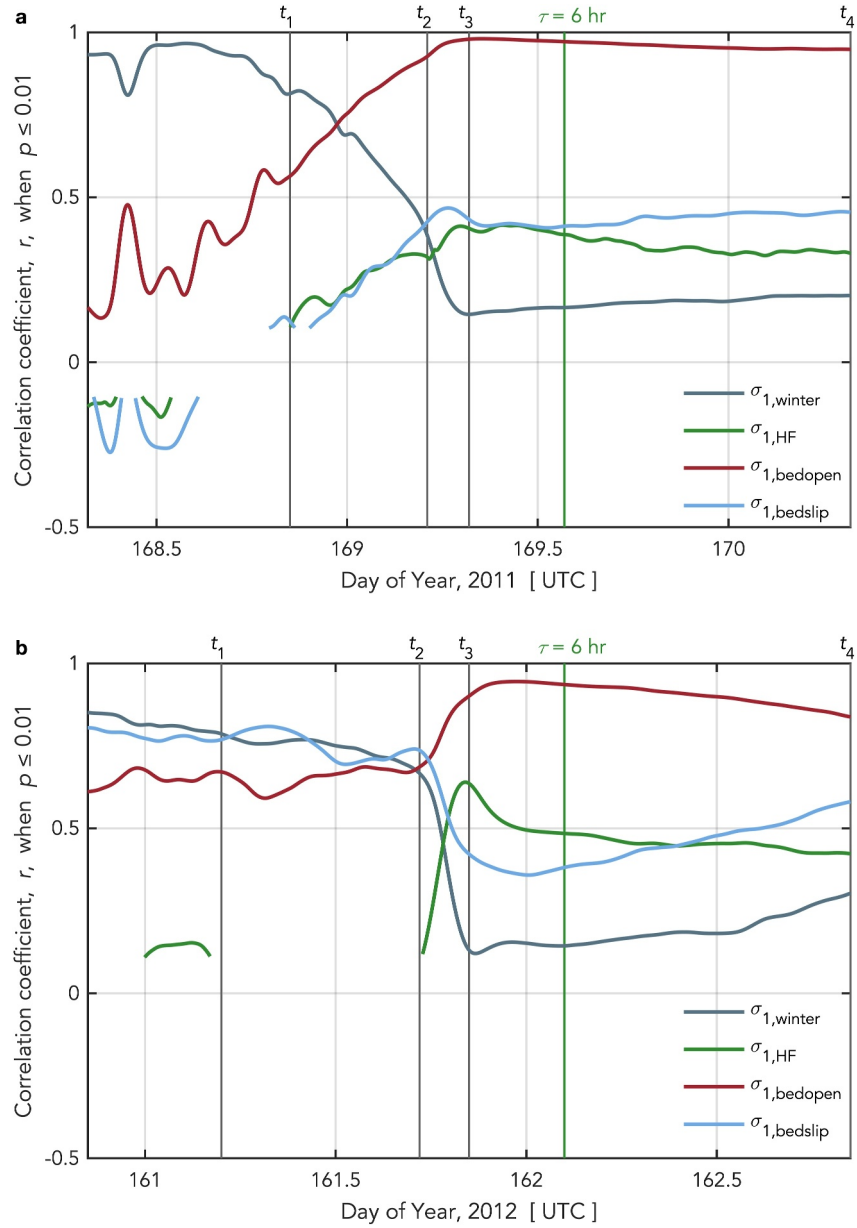

Figure 7. Variability in modeled total stress σ_1 explained by individual stress components during the 2011 and 2012 L1A drainages. Correlation coefficient r between (gray) $\sigma_{1,winter}$ and σ_1; (green) $\sigma_{1,HF}$ and σ_1; (red) $\sigma_{1,bedopen}$ and σ_1; and (blue) $\sigma_{1,bedslip}$ and σ_1 during the (a) 2011 and (b) 2012 L1A drainages. Values are plotted only when p-values of the linear regression are ≤0.01. The regression sample size is 625: the number of σ_1 values within the $x \leq |6|$ km and $y \leq |6|$ km region in Figure 6. Event timepoints t_{1-4} and the approximate lower bound of 6-hr for the Maxwell time τ for glacial ice are shown as vertical lines with labels along the upper x-axes.

are most comparable to $\sigma_{1,lake}$ estimates at the time of maximum L1A hydro-fracture opening (e.g., Figure 3g), with the exception that idealized simulations in Figure 8; Figure S7 and S8 in Supporting Information S1 do not include stresses generated by a hydro-fracture opening term (e.g., Figure 4i).

While rapid drainages at L1A (Das et al., 2008; Lai et al., 2021; Stevens et al., 2015) and other lakes (Chudley et al., 2019; Doyle et al., 2013; Tedesco et al., 2013) result in coincident vertical and horizontal deformation driven by a combination of basal cavity opening and basal slip, idealized scenarios allow us to partition contributions to σ_1 from these different sources explicitly (Figures 4 and 8). For $V \geq 0.005$ km^3 and $H \geq 1{,}000$ m, a basal cavity opening of an equivalent volume to V yields a contribution to σ_1 approximately four times larger than

21699011, 2024, 5, Downloaded from https://agupubs.onlinelibrary.wiley.com/doi/10.1029/2023JF007481 by Test, Wiley Online Library on [27/06/2024]. See the Terms and Conditions (https://onlinelibrary.wiley.com/terms-and-conditions) on Wiley Online Library for rules of use; OA articles are governed by the applicable Creative Commons License

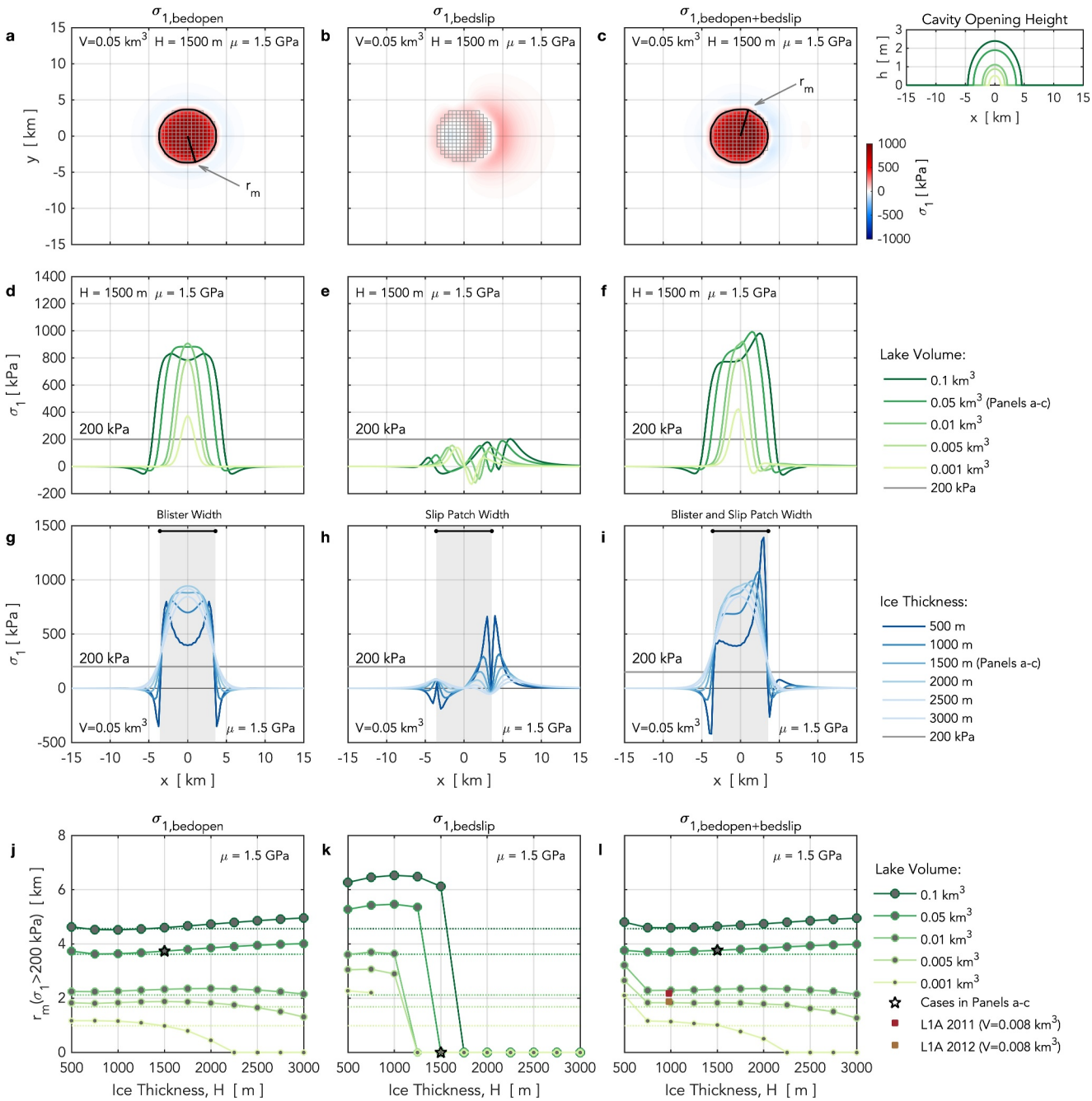

Figure 8. Idealized lake-drainage simulations for a range of ice-sheet thicknesses and drainage volumes. Maximum horizontal principal stress σ_1 from imposed distributions of (a) basal cavity opening, (b) basal slip, and (c) both basal cavity opening and slip for idealized scenarios where H = 1,500 m, V = 0.05 km^3, and μ = 1.5 GPa. The direction of imposed basal slip in all simulations is in the $-x$ direction. Black lines show 200-kPa contour in σ_1. Gray arrows point to r_m, the distance to the farthest up-flowline point from the origin where σ_1 > 200 kPa. Basal-plane subfaults with non-zero basal cavity opening and basal slip are shown with gray squares. Modeled value of σ_1 for different (d)–(f) V and (g)–(i) H along y = 0 km in panels (a–c). Cavity opening height h (imposed as basal cavity opening) for the five values of V shown at the top right. (j–l) (circles) Ice thickness H versus r_m for the full parameter space in H and V for μ = 1.5 GPa. Dotted lines show radius of imposed basal cavity opening R for the five values of V. (squares, panel l) Estimates of r_m at the time of maximum hydro-fracture opening during the 2011 and 2012 L1A drainages (H = 980 m, V = 0.008 km^3) for μ = 1.5 GPa. Stresses from idealized lake-drainage simulations where μ = 0.32 GPa and μ = 3.9 GPa are shown in Figures S7 and S8 of Supporting Information S1.

21699011, 2024, 5, Downloaded from https://agupubs.onlinelibrary.wiley.com/doi/10.1029/2023JF007481 by Test, Wiley Online Library on [27/06/2024]. See the Terms and Conditions (https://onlinelibrary.wiley.com/terms-and-conditions) on Wiley Online Library for rules of use; OA articles are governed by the applicable Creative Commons License

21699011, 2024, 5, Downloaded from https://agupubs.onlinelibrary.wiley.com/doi/10.1029/2023JF007481 by Test, Wiley Online Library on [27/06/2024]. See the Terms and Conditions (https://onlinelibrary.wiley.com/terms-and-conditions) on Wiley Online Library for rules of use; OA articles are governed by the applicable Creative Commons License

the contribution from 0.5 m of down-flow (i.e., in the $-x$ direction) basal slip (Figures 8a and 8b). When both cavity opening and slip are included, σ_1 remains dominated by stress contributions from basal cavity opening, with basal-slip contributions resulting in larger σ_1 at the up-flow edge of the slip patch (Figures 8c and 8f). This idealized result is consistent with σ_1 spatial patterns during L1A drainages, where maximum σ_1 values occur in regions of basal cavity opening and, to a lesser extent, basal slip within the first day following hydro-fracture opening (Figure 6).

For a given ice-sheet thickness H of 1,500 m, lake-drainage volume V exhibits a strong control on σ_1 for simulations with just basal cavity opening, with the most tensile and most compressive values of σ_1 generally increasing with increasing V (Figure 8d). For a lake volume V of 0.05 km^3, H does not exhibit a strong control on the maximum tensile values of σ_1, or radial extent of tensile σ_1, when $H \geq 1{,}500$ m (Figures 8g–8i). Along-flow asymmetries in $\sigma_{1,\text{bedopen+bedslip}}$ are apparent when $H \leq 1{,}000$ m, but are greatly reduced when $H \geq 2{,}000$ m (Figure 8i).

We consider inter-lake stress-coupling length scales in the up-flow direction for the idealized scenarios using the metric r_m: the distance to the farthest point inland from the blister center (i.e., the origin) where $\sigma_1 > \sigma_c$ (Figures 8a and 8c). Variation in V exhibits a stronger control on r_m than the tested variation in H, except for the smallest value of V(0.001 km^3) where r_m decreases to zero with increasing H (Figures 8j–8l). For simulations with just basal slip, modeled σ_1 values do not exceed σ_c when $H \geq 1{,}750$ m, for any value of V (Figure 8k). For simulations with basal cavity opening and slip, r_m remains relatively constant for a given V when $H \geq 750$ m and $V \geq 0.005$ km^3 (Figure 8l). Comparing these idealized simulations to $\sigma_{1,\text{lake}}$ estimates at maximum L1A hydro-fracture opening (Figure 3g; Figure S1g in Supporting Information S1), we find that L1A drainages ($V = \sim 0.008$ km^3; $H = 980$ m) have an r_m of 2.2 km in 2011 and 1.9 km in 2012 in the up-flow direction for $\mu = 1.5$ GPa. These distances are roughly the distance from the L1A lake center to the eastern L1A lake margin and compare well with an r_m value of 2.3 km for the idealized simulation with $V = 0.01$ km^3, $H = 1{,}000$ m, and $\mu = 1.5$ GPa (Figure 8l).

Values of r_m are much smaller for idealized simulations with $\mu = 0.32$ GPa (Figure S7l in Supporting Information S1) than for those with $\mu = 1.5$ GPa, and slightly larger for those with $\mu = 3.9$ GPa (Figure S8l in Supporting Information S1). Across all μ and V for $H \geq 750$ m, values of r_m are no more than ~1 km larger than the radius of imposed basal cavity opening and basal slip R (Figure 8l; Figures S7l and S8l in Supporting Information S1). For simulations with $\mu = 0.32$ GPa, values of r_m are all smaller than R (Figure S7l in Supporting Information S1).

While r_m estimates for the 2011 and 2012 L1A drainages are generated from ice-sheet surface displacements from melt injection to a topographically variable ice-sheet bed (Figure 2a), the idealized simulations use a radially symmetric blister geometry derived for a flat bed (Lai et al., 2021). Previous theoretical work suggests that gradients in hydraulic potential for the largest bed slopes in our study area (~0.04) are not large enough to affect the initial blister-relaxation dynamics, when compared to the elastic stresses of the deformed ice sheet due to the blister (Lai et al., 2021).

5. Discussion

5.1. Stress Coupling Between Neighboring Supraglacial Lake Basins

Using in situ observations of ice-sheet surface deformation at neighboring supraglacial lake basins spaced 2–4 km apart in the mid-ablation zone, we find that lakes can be placed in either tensional or compressional surface strain-rate and stress states during and immediately following the rapid drainage of a neighboring lake. The sense of surface-stress change is highly dependent on where surface uplift caused by the central lake drainage occurs. Hydro-fracture opening, basal-cavity opening, and basal-slip distributions caused by the L1A rapid drainage place the L1C basin located 3.5 km to the north in compression in roughly the orientation of the L1C hydro-fracture scarp (Figure 6; Figure S6 in Supporting Information S1). Together with the relatively more compressive background winter stresses in the L1C basin caused by large-scale flow patterns (Figure 3e), this stress change likely hinders the reactivation of existing fractures, and prevents the opening of new fractures that otherwise might lead to hydro-fracture initiation beneath L1C. These estimates of changes in ice-sheet surface stress are consistent with the non-drainage of L1C in 2011, 2012, and other years in the study period (Figure 1b).

By contrast, the L1A drainages place the L1B basin located 2 km to the south in tension relative to the L1B hydro-fracture scarp (Figure 6; Figure S6 in Supporting Information S1), promoting fracture opening and hydro-fracture

21699011, 2024, 5, Downloaded from https://agupubs.onlinelibrary.wiley.com/doi/10.1029/2023JF007481 by Test, Wiley Online Library on [27/06/2024]. See the Terms and Conditions (https://onlinelibrary.wiley.com/terms-and-conditions) on Wiley Online Library for rules of use; OA articles are governed by the applicable Creative Commons License

initiation beneath L1B. Though a lake did not form in the L1B basin in 2011, our analysis suggests that in years when both L1A and L1B form and drain close in time (e.g., 2012; Figure 5), the L1A drainage can lead to the concentration of tensional stresses in the L1B basin. Together with the relatively more tensional background winter stresses in the L1B basin (Figure S1e in Supporting Information S1), stress coupling between L1A and L1B potentially explains why L1A has drained synchronously (i.e., within 1–3 days) with L1B in 50% of the years that both lakes formed from 2000 to 2023, but has only drained synchronously with L1C in 12.5% of the years that both lakes formed over the same time period (Figure 1b). Thus, based on our in situ observations in 2011 and 2012 and a 24-year record of lake-drainage timing, a rapid drainage of one lake may drive stress changes that promote hydro-fracture initiation and drainage in some neighboring basins, while simultaneously inhibiting hydro-fracture initiation and drainage in others.

The sign difference in the stress changes between the L1B and L1C basins is largely due to the geometry of ice-sheet uplift, on the southern side of the L1A lake-draining fracture, generated by basal cavity opening (Figures 6c and 6k). The fact that basal cavity opening occurs in this location is likely due to the specific lakes that drain (i.e., L1A and L1B) early in the melt season (Stevens et al., 2016), the lower basal topography beneath the L1A and L1B basins (Figure 2a), and the resulting hydraulic gradient in the subglacial drainage system, which drives subglacial water flow from beneath L1A toward the southwest (Chu et al., 2016; Stevens et al., 2018). As time progresses during the 2011 and 2012 drainages, spatial variability in σ_1 is increasingly explained by $\sigma_{1,\text{bedopen}}$, the stress component caused by basal cavity opening (Figure 7). Similarly, basal uplift is the dominant precursor signal observed in the hours leading up to hydro-fracture initiation (Chudley et al., 2019; Das et al., 2008; Doyle et al., 2013; Stevens et al., 2015), likely because ice-sheet surface vertical displacements (i.e., the doming of the ice-sheet surface) caused by basal cavity opening generate larger tensile stresses than basal slip on these elastic timescales (Figure 4). Our idealized lake-drainage simulations allow an explicit partitioning of contributions to σ_1 from basal cavity opening and basal slip, and confirm that tensional surface stresses at the time of initial blister formation are predominantly caused by ice-sheet uplift (Figure 8).

5.2. Likelihood of Elastic Stress Coupling Between Distant Supraglacial Lakes

It has been proposed that hydro-fracture beneath lakes in the upper ablation zone, up to ~80 km inland, may be triggered by the drainage of lakes near the ice-sheet margin through a stress-coupling mechanism (Christoffersen et al., 2018) associated with a change in force balance following the loss of basal traction. In this framework, changes in the ice-sheet stress field result from the response of the viscous material to changes in the balance of driving and resisting stresses; and, it is the immediate ice response to the change in force balance that is invoked to explain apparent triggering of cascading lake drainage by "tensile shock and fracture" (Christoffersen et al., 2018). Similarly, Hoffman et al. (2018) propose that the loss of basal traction associated with passage of subglacial water, initially injected by lake drainages, changes surface stresses on the timescale of the water passage (<1 day) to allow surface fracturing and moulin formation, with the change in stress again representing a response to the change in force balance controlling viscous flow. As we have demonstrated here, a different mechanism, the elastic deformation associated with lake drainage to the ice-sheet bed, can produce large changes in the surface stress field, sufficient to trigger drainage at nearby lakes. These stress changes, being elastic, are nearly instantaneous, and will affect the ice sheet over timescales similar to those considered by Christoffersen et al. (2018) and Hoffman et al. (2018). Here, we examine the likelihood that elastic stress coupling might lead to triggering between distant lakes. We are cognizant that longitudinal-coupling length scales for viscous deformation of a fully relaxed ice sheet are likely to be longer than the elastic length scales (Kamb & Echelmeyer, 1986; Price et al., 2008; Sergienko, 2013).

Our observations from the mid-ablation zone suggest that, while elastic stress coupling may trigger hydro-fracture-driven drainages at other nearby lakes within the region of ice-sheet uplift driven by basal cavity opening, elastic stress coupling is unlikely to trigger drainages at distal lakes. We find the extent of basal cavity opening—and not ice thickness—to be the primary control on where regions of highly tensile σ_1 occur (Figures 6e, 6m, and 8). Following the two L1A drainages, regions of highly tensile σ_1 track the extent of basal cavity opening, which advances over time from the region beneath L1A and L1B to the southwest (Figures 6e and 6m). The limited extent of our GPS array prevents further investigation of whether L1A drainages can sufficiently modulate elastic surface stresses to trigger hydro-fracture-driven drainages of lakes farther down the subglacial hydraulic catchment than L1B as the drained water passes by. In our study area, two GPS stations (FL01 and FL02) located ~9 km and ~16 km down-flow from L1A in 2012 show no anomalous along-flow, across-flow, or

21699011, 2024, 5, Downloaded from https://agupubs.onlinelibrary.wiley.com/doi/10.1029/2023JF007481 by Test, Wiley Online Library on [27/06/2024]. See the Terms and Conditions (https://onlinelibrary.wiley.com/terms-and-conditions) on Wiley Online Library for rules of use; OA articles are governed by the applicable Creative Commons License

vertical displacements during or following the 2012 L1A drainage, apart from a change in along-flow velocity (Figure 2). Because the inferred region of basal cavity opening and highly tensile σ_1 expanded to the southwest of L1A (Figures 6e and 6m), we hypothesize that it is most likely that the drained lake water flowed to the southwest, following hydraulic gradients in the subglacial drainage system (Chu et al., 2016; Stevens et al., 2018), thereby avoiding FL01 and FL02.

Within the extent of the GPS array in the up-flow direction from L1A, regions of highly tensile σ_1 extend <1 km up-flow of the eastern L1A lake margin (Figures 6e and 6m; Movies S1 and S2). We expect lower tensile stresses in this region because GPS stations here record little to no uplift during drainage events (Figure 2d) (Stevens et al., 2015). A single GPS station (FL06) located ∼26 km up-flow from L1A in 2012 shows no anomalous displacements during or in the days following the 2012 L1A drainage (Figure 2). Together, these observations suggest that the up-flow, elastic stress-coupling length scale is short: no more than 3 km inland of the center of the draining lake (Figures 6e and 6m).

The short up-flow stress-coupling length scale of a few ice thicknesses suggested by stresses modeled from our in situ observations is consistent with the idealized simulations for a wider range of lake volumes and ice-sheet thicknesses. Across all tested μ and V for simulations where $H \geq 750$ m, values of r_m (the distance to the farthest point inland from the origin where $\sigma_1 > \sigma_c$) are no more than ∼1 km greater than the radius of imposed basal cavity opening and basal slip (Figure 8l; Figures S7l and S8l in Supporting Information S1). These idealized simulations show that—for this range in ice-sheet thickness—the first-order control on elastic stress-coupling length scales is the region of the bed over which basal cavity opening occurs. Within the initial hours following lake drainage, this region is limited to the size of a fluid-filled blister that can be generated by the volume of the drained lake (Hewitt et al., 2018; Lai et al., 2021; Tsai & Rice, 2010).

The idealized simulations highlight the importance of the interplay between basal cavity opening and basal slip in driving ice-sheet deformation and stresses. The spatial pattern and magnitude of σ_1 generated by basal slip alone (Figures 4k and 8b) is strongly modified by the addition of basal cavity opening (Figures 4l and 8c) across all simulated ice thicknesses and lake volumes. This finding indicates that attempts to model stresses ensuing from lake drainages that do not consider vertical displacements (e.g., Christoffersen et al., 2018; Hoffman et al., 2018) may exclude a leading source of tensional surface stress in the drainage region and along the path of a propagating bolus of water, and mischaracterize the spatial pattern of surface stress. The importance of the contribution from cavity opening also suggests that frameworks that require ice-sheet surface displacements over seconds-to-weekly timescales to be explained exclusively by changes in basal sliding may incorrectly estimate the amount of sliding occurring at the bed, and thus may overestimate the importance of basal sliding in driving tensile surface stresses. To better understand the likelihood of stress coupling between distant supraglacial lakes, ice-sheet stress estimates should consider both horizontal and vertical ice-sheet deformation (e.g., Pimentel & Flowers, 2011; Dow et al., 2015), and an evolving basal blister and slip distribution due to drainage-imposed changes in subglacial hydrology. Here, we have focused on constraining elastic deformation during the day of the initial drainage; however, the consideration of viscoelastic deformation and temporal evolution of basal slip are needed to fully understand stress evolution following lake drainages. While our observations and models show that elastic stress changes due to lake drainage can be effective in triggering additional drainages nearby, we find that they are unlikely to trigger drainages at lakes more than a few kilometers from the initially drained lake.

5.3. Rotations in Surface Stress Orientation

For faults in the Earth's lithosphere, rotations of principal stresses occur during earthquakes and imply background differential stresses that are on the order of earthquake stress drops (Hardebeck & Okada, 2018). We observed similar stress changes during the lake drainages, where background ice-sheet surface stresses are low compared to the stresses induced by the lake drainage (Figure 6). During earthquakes, stress orientations rotate at most 20° from pre-event stress orientations (Hardebeck & Okada, 2018). We observed much larger stress rotations, on the order of 25–52°, within the L1C basin, and 76–111° within the L1B basin, in both years studied (Figure S6 in Supporting Information S1). These rotations are calculated relative to a background stress orientation set by winter-velocity fields (Figure 6a). We are not aware of any previous observations of rotations in ice-sheet surface stresses of this magnitude calculated using both horizontal and vertical ice-sheet displacements. Rotations in principal stresses were identified in modeled ice-sheet surface stresses obtained from variations in horizontal velocities observed in the Pâkitsoq region in western Greenland (Hoffman et al., 2018).

21699011, 2024, 5, Downloaded from https://agupubs.onlinelibrary.wiley.com/doi/10.1029/2023JF007481 by Test, Wiley Online Library on [27/06/2024]. See the Terms and Conditions (https://onlinelibrary.wiley.com/terms-and-conditions) on Wiley Online Library for rules of use; OA articles are governed by the applicable Creative Commons License

In the months to years following earthquakes, crustal stresses rotate back to the pre-event stress field, which is set by long-term plate motion (Hardebeck & Okada, 2018). A rotation back to pre-event stress orientations must also occur following the lake drainages, as ice flow is driven, on larger scales, by ice-sheet geometry (Cuffey & Paterson, 2010). Inter-station horizontal strain rates return to pre-event values within a few hours following the drainages (Figure 5 and Figure S2 in Supporting Information S1), indicating that ice-flow quickly reverts to its pre-drainage direction. Ice-sheet-surface vertical deformation, however, takes ∼10 days in 2011 and ∼2 days in 2012 (Figure 2d) to relax to pre-event heights (Lai et al., 2021), delaying the return to pre-event stress orientations. Over these time-scales, NIF-derived estimates are inappropriate for estimating stresses; methodologies which incorporate viscoelastic deformation are required to quantify stress orientation rotations back to pre-event directions following rapid lake drainages.

5.4. Considering Hydro-Fracture Likelihood Within a Triggering Framework

Our modeled estimates of stress invite the consideration of hydro-fracture likelihood within frameworks developed to investigate triggering relationships between terrestrial earthquakes (Harris, 1998; Scholz, 2019; Stein, 1999). Here, we apply this framework as a lens for interrogating the utility of stress-threshold criteria that have emerged in recent years for identifying "triggered" supraglacial lake drainages (Andrews et al., 2018; Christoffersen et al., 2018; Hoffman et al., 2018; Poinar & Andrews, 2021; Stevens et al., 2015; Williamson et al., 2018).

During L1A drainages, the L1C basin experiences a change to more compressional surface stresses and L1C does not drain in either year, providing strong support for the importance of the direction of stress change (Harris, 1998). For the importance of the amount of stress, in this study, we considered 200 kPa as an estimate for the yield stress of glacial ice σ_c, above which we expect surface fractures to open (van der Veen, 1998, 2007; Weertman, 1973). We can use σ_1 estimates at the two draining lakes in our study to test this chosen σ_c. At L1A hydro-fracture initiation (t_2), L1A σ_1 values are 288 kPa in 2011 and 160 kPa in 2012 when $\mu = 1.5$ GPa (Figures 6i and 6q). In 2012, when L1B also drains via hydro-fracture, L1B σ_1 values surpass these two L1A $\sigma_1(t_2)$ values (Figure 6q), supporting a tensile stress-threshold criterion for hydro-fracture initiation for the two lakes. Increasing μ from 1.5 to 3.9 GPa more than doubles the estimates of L1A $\sigma_1(t_2)$, but L1A $\sigma_1(t_2)$ does not reach the 1 MPa order-of-magnitude threshold suggested by Ultee et al. (2020) in either year (Figures 6i and 6q).

The value of stress—or stress change—needed to initiate hydro-fracture, however, may also depend on how close the proto-fracture is to failure (Stein, 1999), which may differ between lake basins. If one or multiple fractures already exist in the lake basin, a lower σ_c for initiating hydro-fracture is expected. The recurring fracture through L1A is likely to be near this end member, as some portion of this fracture has reactivated nearly annually since at least 2006 (Das et al., 2008). If hydro-fracture-driven drainage occurs through undamaged ice, the proto-fracture is further from failure and a higher σ_c is required for fracture initiation. This end member may be relevant for lakes like L1C, which had a 7-year stretch with no drainages from 2009 to 2016 (Figure 1b). By attempting to constrain σ_c using observations of a fracture plane near failure, we risk defining σ_c to be too low for (a) lakes at equivalent elevations with a lower drainage frequency via hydro-fracture and (b) lakes at higher elevations where ice is currently less damaged (Howat et al., 2013). Setting σ_c too low and applying the same σ_c across different lake basins would lead to an over prediction of hydro-fracture-driven drainages.

In sum, using a fixed stress threshold as the criterion for predicting whether a particular hydro-fracture-driven drainage could be triggered by another lake drainage may not be very useful, especially if this criterion is applied independent of lake-specific factors including, but not limited to, the degree of ice damage, the advection and/or temporal evolution of surface-to-bed meltwater pathways, and the temporal spacing of hydro-fracture events along repeatedly used fracture planes. In the potentially analogous case of triggering relationships between earthquakes, various perturbing stresses have been observed to trigger or not to trigger earthquakes (Pollitz et al., 2012; Prejean & Hill, 2014). The full picture for triggering relationships between lake drainages is likely more complicated than can be treated in this study of three lakes. However, our demonstration that the drainage of one lake can either promote or inhibit drainage of neighboring lakes via hydro-fracture points toward the use of a framework that quantifies the increased (or decreased) likelihood of hydro-fracture initiation, rather than the exclusive application of a uniform stress threshold.

21699011, 2024, 5, Downloaded from https://agupubs.onlinelibrary.wiley.com/doi/10.1029/2023JF007481 by Test, Wiley Online Library on [27/06/2024]. See the Terms and Conditions (https://onlinelibrary.wiley.com/terms-and-conditions) on Wiley Online Library for rules of use; OA articles are governed by the applicable Creative Commons License

5.5. Open Challenges in Determining Lake-Drainage Mechanisms

Several processes in addition to stress-coupling triggers for hydro-fracture-driven drainage likely contribute to temporal and spatial clustering of lake drainage (Yang & Smith, 2016). In this section, we use examples from the lakes in our study to illustrate how lake-filling synchronicity and temporal aliasing in remote-sensing observations can lead to apparent clustering in which the lake-drainage mechanism is unrelated to stress transmission between lake basins. Correctly differentiating between the various processes, and a clear understanding of data limitations that can lead to the observation of apparent drainage clusters, is required to apply the mechanism of elastic stress coupling observed in this study to the evaluation of hydro-fracture-driven drainage dynamics of other populations of lakes.

In our study area, the three lake basins lie at similar elevations and fill based on similar surface-melt rates. Similar rates of lake filling can lead to, or facilitate, drainage synchronicity for lakes of similar basin volumes and supraglacial catchment areas (Yang & Smith, 2016). For example, from 2000 to 2023, lake-filling onset synchronicity in 88% of years and drainage synchronicity in 12.5% of years was observed between L1A and a lake 6 km to the northeast: L1D (68.77°N, 49.44°W; lake "B" in Kingslake et al. (2015); Table S2 in Supporting Information S1). In most years, a prominent outflow stream exits from the western margin of L1D before flowing into L1C (Kingslake et al., 2015) or into a crevasse field to the north (Figures 1c–1f), indicating that L1D drains via overspill mechanisms not associated with surface-stress changes. Interpreting L1D and L1A synchronous drainages as mechanistic examples of stress coupling between the two lakes—or any lakes that drain synchronously via outflow streams (e.g., Christoffersen et al., 2018)—would be inaccurate.

Compared to in situ GPS observations, temporal aliasing in remote-sensing observations of horizontal strain rates (Poinar & Andrews, 2021) and lake-drainage dates (Yang & Smith, 2016) pose significant challenges for confidently assessing lake-drainage mechanisms. Our GPS data constrain the duration of lake-drainage-induced strain rates outside of background conditions ($>|0.05|\ yr^{-1}$) in both years to be <4 hr in all three lake basins (Figure 5 and Figure S2 in Supporting Information S1). Thus, the duration of horizontal strain-rate coupling during a rapid lake drainage event occurs over durations that are almost always too short to be observed in remotely sensed surface velocities (Poinar & Andrews, 2021). Similarly, optical satellite-imagery records with temporal image spacing longer than the duration of rapid lake drainage (∼2–6 hr) will typically be insufficient to distinguish between hydro-fracture-driven drainages and overspill drainages (Fitzpatrick et al., 2014; Morriss et al., 2013; Selmes et al., 2011). With roughly a third of days being cloudy during the melt season (Cooley & Christoffersen, 2017), drainage-date catalogs compiled from optical images will almost always provide temporally aliased records of lake-drainage dates. Determining the mechanisms of individual or temporally clustered lake drainages from such records is problematic (Poinar & Andrews, 2021; Williamson et al., 2018), unless all post-drainage basins are inspected for evidence of drainage via overspill versus hydro-fracture (e.g., Selmes et al., 2011). Regular synthetic aperture radar (SAR) coverage can be used to monitor lake filling and draining through clouds, with a consistent temporal sampling of 6 days (Lemos et al., 2018), but our GPS observations suggest that this frequency is still too coarse.

The dense spatial sampling of our GPS array captures differences in ice-sheet horizontal and vertical deformation during lake-drainage events that occur over inter-station baselines as short as 2–3 km (Figures 2b–2d), indicating that the length scale for coherent surface deformation in our study area can be as short as ∼2 ice thicknesses. We observe sign differences in strain rates (Figure 5 and Figure S2 in Supporting Information S1) and modeled stresses (Figure 6) over similar distances. With a reduced spatial density of observations, such as that we would obtain from strain-rate estimates across two lake basins (Figure S5 in Supporting Information S1), the basin-specific strain-rate patterns observed to align with temporally evolving stresses would be obscured. These observations elucidate a critical point for studying inter-lake drainage dynamics: multiple GPS observations are needed at locations surrounding individual lake basins and at locations along subglacial-flood pathways between lake basins to accurately calculate strain rates and stresses between and within neighboring basins. Arrays that are predominantly oriented along the flowline are not as well suited for the study of inter-lake drainage dynamics (Poinar & Andrews, 2021).

Finally, remotely sensed horizontal surface velocities cannot fully resolve components of elastic stress driven by ice-sheet uplift, which we find to be the strongest predictor of σ_1 during drainages (Figure 7). Recent advances in the analysis of differential SAR interferometry (DInSAR) Line-of-Sight velocity fields have constrained both vertical and horizontal displacement fields during winter episodes of subglacial water movement beneath the

21699011, 2024, 5, Downloaded from https://agupubs.onlinelibrary.wiley.com/doi/10.1029/2023JF007481 by Test, Wiley Online Library on [27/06/2024]. See the Terms and Conditions (https://onlinelibrary.wiley.com/terms-and-conditions) on Wiley Online Library for rules of use; OA articles are governed by the applicable Creative Commons License

Greenland Ice Sheet, highlighting that a substantial component of surface deformation due to this water movement is vertical (Andersen et al., 2023; Maier et al., 2023). However, InSAR-based approaches are unable to coherently observe ice-sheet surface deformation in the ablation zone during the melt season, as surface ablation contributes to the vertical component of motion observed by DInSAR Line-of-Sight velocity fields (Andersen et al., 2023).

6. Conclusions

A mechanistic understanding of meltwater pathways connecting the surface of the Greenland Ice Sheet to the bed is required to estimate where future pathways are likely to form. Hydro-fracture beneath supraglacial lakes is one way to create new surface-to-bed pathways within and near lake basins. In this study, we have focused on a group of three lakes that form <4 km apart in the ablation zone of the western margin of the Greenland Ice Sheet, all of which experience drainage via hydro-fracture in some years. We investigate whether elastic stress transmission following the drainage of one lake is sufficient to induce hydro-fracture-driven drainages of other lakes. We find that, when the central lake drains via hydro-fracture, the two neighboring basins are placed in, respectively, tensional and compressional surface stress relative to their individual basin hydro-fracture scarp orientations. In the basin receiving increased tensional stress, hydro-fracture initiation and drainage is thus promoted, while in the basin receiving compressional stress, fracture and drainage are inhibited. In both years for which in situ observations are available, the sense of surface-stress change is highly dependent on where surface uplift caused by basal cavity opening occurs following drainage of the central lake.

Our estimates of changes in ice-sheet surface stress are consistent with the drainage timing of the three lakes from 2000 to 2023, with the lake that is placed in tension draining close in time to the central lake four times as often as the lake placed in compression. We find that elastic stress changes caused by basal-cavity opening provide a physical explanation for these lakes' temporally clustered, hydro-fracture-driven drainages and their regular triggering behavior. However, changes to the stress field during and immediately following drainages are spatially complex, and we find a short, up-flow stress-coupling length scale of no more than a few ice thicknesses, indicating that elastic deformation during a rapid lake drainage is unlikely to affect stresses far inland, and unlikely to trigger distal inland lakes to drain via hydro-fracture. Additional in situ observations between lake basins located farther apart from one another, but still within the same subglacial hydrologic catchment, would enable further testing of this hypothesis. Pairing such observations with ice-sheet stress estimates that consider both (a) the horizontal and vertical ice-sheet deformation characteristics of lake drainages, and (b) an evolving basal blister and slip distribution due to drainage-imposed changes in subglacial hydrology, could further constrain the length scales of stress and the potential hydrologic linkages between lower- and upper-elevation lake basins. In addition, our findings highlight the need for greater attention to identifying the drainage mechanism—hydro-fracture versus basin overspill—in catalogs of lake-drainage dates in order to justify extending the observation of stress transmission between lake basins shown in this local study to the evaluation of hydro-fracture-driven drainage dynamics of other lakes.

Conflict of Interest

The authors declare no conflicts of interest relevant to this study.

Data Availability Statement

Sentinel-2 Imagery from the European Space Agency were accessed via the U.S. Geological Survey Earth Explorer (https://earthexplorer.usgs.gov); the file names of images used here are listed in Table S3 of Supporting Information S1. TerraSAR-X velocity data are archived at the National Snow and Ice Data Center (https://nsidc.org/data/nsidc-0478/versions/2; Joughin et al., 2015). GPS data are archived at the GAGE Facility operated by the EarthScope Consortium (https://www.unavco.org/data/doi/10.7283/T5222SJK; Das et al., 2018). The Cooley and Christoffersen (2017) drainage-date catalog for the North Lake region (Table S1 in Supporting Information S1) was obtained from S. Cooley via personal communication. Data and model output underlying figures and videos presented in this study are archived in a Zenodo repository (https://doi.org/10.5281/zenodo.10650188;

Stevens & Larochelle, 2024). Multiple figures presented in this study use the "Dock at Eel Pond" palette of PaletteWoodsHole (https://github.com/shu251/PaletteWoodsHole).

Acknowledgments
Support was provided by the National Science Foundation's Office of Polar Programs (NSF-OPP) and National Aeronautics and Space Administration's (NASA's) Cryospheric Sciences Program through ARC-0520077, ARC-1023364, and NNX10AI30G to S.B.D. and M.D.B.; OPP-1838410 to M.D.B.; ANS-2003464 to M.N.; OPP-2235051 to C.-Y.L.; and ARC-0520382, ARC-1023382, and NNX10AI33G to I.J. L.A.S. acknowledges funding from the John Fell Oxford University Press Fund and the UK Natural Environment Research Council (NE/Y002369/1). Logistical and instrumental support was provided by UNAVCO, PASSCAL, and CH2MHILL Polar Field Services. We thank J. Carmichael, L. Kehrl, T. Moon, K. Poinar, and D. Shean for their assistance in the field. We thank J.-A. Olive and the Geodynamics Discussion Group for early conversations on this work. We thank four anonymous reviewers for their contributions to improving the readability of the manuscript. Any use of trade, firm, or product names is for descriptive purposes only and does not imply endorsement by the U.S. Government.

References

Alley, R. B., Dupont, T. K., Parizek, B. R., & Anandakrishnan, S. (2005). Access of surface meltwater to beds of sub-freezing glaciers: Preliminary insights. *Annals of Glaciology*, *40*(1), 8–14. https://doi.org/10.3189/172756405781813483

Andersen, J. K., Rathmann, N., Hvidberg, C. S., Grinsted, A., Kusk, A., Merryman Boncori, J. P., & Mouginot, J. (2023). Episodic subglacial drainage cascades below the Northeast Greenland Ice Stream. *Geophysical Research Letters*, *50*(12), e2023GL103240. https://doi.org/10.1029/2023gl103240

Andrews, L. C., Hoffman, M. J., Neumann, T. A., Catania, G. A., Lüthi, M. P., Hawley, R. L., et al. (2018). Seasonal evolution of the subglacial hydrologic system modified by supraglacial lake drainage in western Greenland. *Journal of Geophysical Research: Earth Surface*, *123*(6), 1479–1496. https://doi.org/10.1029/2017JF004585

Bevis, M., Wahr, J., Khan, S. A., Madsen, F. B., Brown, A., Willis, M., et al. (2012). Bedrock displacements in Greenland manifest ice mass variations, climate cycles and climate change. *Proceedings of the National Academy of Sciences of the United States of America*, *109*(30), 11944–11948. https://doi.org/10.1073/pnas.1204664109

Budd, W. F., & Jacka, T. H. (1989). A review of ice rheology for ice sheet modeling. *Cold Regions Science and Technology*, *16*(2), 107–144. https://doi.org/10.1016/0165-232x(89)90014-1

Catania, G. A., Neumann, T. A., & Price, S. F. (2008). Characterizing englacial drainage in the ablation zone of the Greenland Ice Sheet. *Journal of Glaciology*, *54*(187), 567–578. https://doi.org/10.3189/002214308786570854

Chase, D. L., Lai, C.-Y., & Stone, H. A. (2021). Relaxation of a fluid-filled blister on a porous substrate. *Physical Review Fluids*, *6*(8), 1–12. https://doi.org/10.1103/physrevfluids.6.084101

Chen, G. (1998). *GPS kinematic positioning for the airborne laser altimetry at Long Valley, California*. Massachusetts Institute of Technology.

Christoffersen, P., Bougamont, M., Hubbard, A., Doyle, S. H., Grigsby, S., & Pettersson, R. (2018). Cascading lake drainage on the Greenland Ice Sheet triggered by tensile shock and fracture. *Nature Communications*, *9*(1), 1–12. https://doi.org/10.1038/s41467-018-03420-8

Chu, W., Creyts, T. T., & Bell, R. E. (2016). Rerouting of subglacial water flow between neighboring glaciers in West Greenland. *Journal of Geophysical Research: Earth Surface*, *121*(5), 1–14. https://doi.org/10.1002/2015JF003705

Chudley, T. R., Christoffersen, P., Doyle, S. H., Bougamont, M., Schoonman, C. M., Hubbard, B., & James, M. R. (2019). Supraglacial lake drainage at a fast-flowing Greenlandic outlet glacier. *Proceedings of the National Academy of Sciences*, *116*(51), 1–10. https://doi.org/10.1073/pnas.1913685116

Cooley, S. W., & Christoffersen, P. (2017). Observation bias correction reveals more rapidly draining lakes on the Greenland Ice Sheet. *Journal of Geophysical Research: Earth Surface*, *122*(10), 1867–1881. https://doi.org/10.1002/2017JF004255

Cuffey, K. M., & Paterson, W. S. B. (2010). *The physics of glaciers* (4th ed.). Elsevier.

Culberg, R., Schroeder, D. M., & Chu, W. (2021). Extreme melt season ice layers reduce firn permeability across Greenland. *Nature Communications*, *12*(1), 2336. https://doi.org/10.1038/s41467-021-22656-5

Das, S. B., Behn, M. D., Joughin, I., & Stevens, L. A. (2018). Greenland fractures 2011–2014, The GAGE facility operated by EarthScope Consortium. *GPS/GNSS Observations Dataset, GPS/GNSS Observations Dataset*. https://doi.org/10.7283/T55T3J80

Das, S. B., Joughin, I., Behn, M. D., Howat, I. M., King, M. A., Lizarralde, D., & Bhatia, M. P. (2008). Fracture propagation to the base of the Greenland Ice Sheet during supraglacial lake drainage. *Science*, *320*(5877), 778–781. https://doi.org/10.1126/science.1153360

Dow, C. F., Kulessa, B., Rutt, I. C., Tsai, V. C., Pimentel, S., Doyle, S. H., et al. (2015). Modeling of subglacial hydrological development following rapid supraglacial lake drainage. *Journal of Geophysical Research: Earth Surface*, *120*(6), 1127–1147. https://doi.org/10.1002/2014JF003333

Doyle, S. H., Hubbard, A. L., Dow, C. F., Jones, G. A., Fitzpatrick, A., Gusmeroli, A., et al. (2013). Ice tectonic deformation during the rapid in situ drainage of a supraglacial lake on the Greenland Ice Sheet. *The Cryosphere*, *7*(1), 129–140. https://doi.org/10.5194/tc-7-129-2013

Fitzpatrick, A. A. W., Hubbard, A. L., Box, J. E., Quincey, D. J., van As, D., Mikkelsen, A. P. B., et al. (2014). A decade (2002–2012) of supraglacial lake volume estimates across Russell Glacier, West Greenland. *The Cryosphere*, *8*(1), 107–121. https://doi.org/10.5194/tc-8-107-2014

Glen, J. W. (1955). The creep of polycrystalline ice. *Proceedings of the Royal Society of London. Series A. Mathematical and Physical Sciences*, *228*(1175), 519–538.

Hardebeck, J. L., & Okada, T. (2018). Temporal stress changes caused by earthquakes: A review. *Journal of Geophysical Research: Solid Earth*, *123*(2), 1350–1365. https://doi.org/10.1002/2017JB014617

Harris, R. A. (1998). Introduction to special section: Stress triggers, stress shadows, and implications for seismic hazard. *Journal of Geophysical Research*, *103*(10), 24347–24358. https://doi.org/10.1029/98jb01576

Herring, T. A., King, R. W., & McClusky, S. C. (2010). *GAMIT Reference Manual: GPS Analysis at MIT, Release 10.4*. Department of Earth, Atmospheric and Planetary Sciences, Massachusetts Institute of Technology.

Hewitt, D. R., Chini, G. P., & Neufeld, J. A. (2018). The influence of a poroelastic till on rapid subglacial flooding and cavity formation. *Journal of Fluid Mechanics*, *855*, 1170–1207. https://doi.org/10.1017/jfm.2018.624

Hobbs, P. V. (1974). *Ice physics*. Clarendon Press.

Hoffman, M. J., Perego, M., Andrews, L. C., Catania, G., Price, S. F., Lüthi, M. P., et al. (2018). Widespread moulin formation during supraglacial lake drainages in Greenland. *Geophysical Research Letters*, *45*(2), 778–788. https://doi.org/10.1002/2017GL075659

Howat, I. M., de la Peña, S., van Angelen, J. H., Lenaerts, J. T. M., & van den Broeke, M. R. (2013). *Brief Communication* "Expansion of meltwater lakes on the Greenland Ice Sheet. *The Cryosphere*, *7*(1), 201–204. https://doi.org/10.5194/tc-7-201-2013

Joughin, I., Das, S. B., Flowers, G. E., Behn, M. D., Alley, R. B., King, M. A., et al. (2013). Influence of ice-sheet geometry and supraglacial lakes on seasonal ice-flow variability. *The Cryosphere*, *7*(4), 1185–1192. https://doi.org/10.5194/tc-7-1185-2013

Joughin, I., Smith, B., Howat, I., & Scambos, T. (2015). *Updated 2018. MEaSUREs Greenland Ice Sheet Velocity Map from InSAR Data, Version 2. 2009/2010 Mosaic*. NASA National Snow and Ice Data Center Distributed Active Archive Center. https://doi.org/10.5067/OC7B04ZM9G6Q

Kamb, B., & Echelmeyer, K. A. (1986). Stress-gradient coupling in glacier flow: I. Longitudinal averaging of the influence of ice thickness and surface slope. *Journal of Glaciology*, *32*(111), 267–284. https://doi.org/10.3189/s0022143000015604

Kingslake, J., Ng, F., & Sole, A. (2015). Modelling channelized surface drainage of supraglacial lakes. *Journal of Glaciology*, *61*(225), 185–199. https://doi.org/10.3189/2015JoG14J158

21699011, 2024, 5, Downloaded from https://agupubs.onlinelibrary.wiley.com/doi/10.1029/2023JF007481 by Test, Wiley Online Library on [27/06/2024]. See the Terms and Conditions (https://onlinelibrary.wiley.com/terms-and-conditions) on Wiley Online Library for rules of use; OA articles are governed by the applicable Creative Commons License

Krawczynski, M. J., Behn, M. D., Das, S. B., & Joughin, I. (2009). Constraints on the lake volume required for hydro-fracture through ice sheets. *Geophysical Research Letters*, *36*(10), L10501. https://doi.org/10.1029/2008gl036765

Lai, C.-Y., Stevens, L. A., Chase, D. L., Creyts, T. T., Behn, M. D., Das, S. B., & Stone, H. A. (2021). Hydraulic transmissivity inferred from ice-sheet relaxation following Greenland supraglacial lake drainages. *Nature Communications*, *12*(3955), 1–10. https://doi.org/10.1038/s41467-021-24186-6

Leeson, A. A., Shepherd, A., Briggs, K., Howat, I., Fettweis, X., Morlighem, M., & Rignot, E. (2015). Supraglacial lakes on the Greenland Ice Sheet advance inland under warming climate. *Nature Climate Change*, *5*(1), 51–55. https://doi.org/10.1038/nclimate2463

Lemos, A., Shepherd, A., McMillan, M., Hogg, A. E., Hatton, E., & Joughin, I. (2018). Ice velocity of Jakobshavn Isbræ, Petermann Glacier, Nioghalvfjerdsfjorden, and Zachariæ Isstrøm, 2015-2017, from Sentinel 1-a/b SAR imagery. *The Cryosphere*, *12*(6), 2087–2097. https://doi.org/10.5194/tc-12-2087-2018

MacFerrin, M. J., Machguth, H., As, D. V., Charalampidis, C., Stevens, C. M., Heilig, A., et al. (2019). Rapid expansion of Greenland's low-permeability ice slabs. *Nature*, *573*(7774), 403–407. https://doi.org/10.1038/s41586-019-1550-3

Maier, N., Andersen, J. K., Mouginot, J., Gimbert, F., & Gagliardini, O. (2023). Wintertime supraglacial lake drainage cascade triggers large-scale ice flow response in Greenland. *Geophysical Research Letters*, *50*(4), e2022GL102251. https://doi.org/10.1029/2022gl102251

Morlighem, M., Williams, C. N., Rignot, E., An, L., Arndt, J. E., Bamber, J. L., et al. (2017). BedMachine v3: Complete bed topography and ocean bathymetry mapping of Greenland from multibeam echo sounding combined with mass conservation. *Geophysical Research Letters*, *44*(21), 11051–11061. https://doi.org/10.1002/2017gl074954

Morriss, B. F., Hawley, R. L., Chipman, J. W., Andrews, L. C., Catania, G. A., Hoffman, M. J., et al. (2013). A ten-year record of supraglacial lake evolution and rapid drainage in West Greenland using an automated processing algorithm for multispectral imagery. *The Cryosphere*, *7*(6), 1869–1877. https://doi.org/10.5194/tc-7-1869-2013

Nye, J. F. (1957). The distribution of stress and velocity in glaciers and ice-sheets. *Proceedings of the Royal Society of London. Series A. Mathematical and Physical Sciences*, *239*, 113–133.

Okada, Y. (1985). Surface deformation due to shear and tensile faults in a half-space. *Bulletin of the Seismological Society of America*, *75*(4), 1135–1154. https://doi.org/10.1785/bssa0750041135

Pimentel, S., & Flowers, G. E. (2011). A numerical study of hydrologically driven glacier dynamics and subglacial flooding. *Proceedings of the Royal Society A: Mathematical, Physical and Engineering Sciences*, *467*(2126), 537–558. https://doi.org/10.1098/rspa.2010.0211

Poinar, K., & Andrews, L. C. (2021). Challenges in predicting Greenland supraglacial lake drainages at the regional scale. *The Cryosphere*, *15*(3), 1–46. https://doi.org/10.5194/tc-15-1455-2021

Poinar, K., Joughin, I., Das, S. B., Behn, M. D., Lenaerts, J. T. M., & van den Broeke, M. R. (2015). Limits to future expansion of surface-melt-enhanced ice flow into the interior of western Greenland. *Geophysical Research Letters*, *42*(6), 1800–1807. https://doi.org/10.1002/2015GL063192

Pollitz, F. F., Stein, R. S., Sevilgen, V., & Bürgmann, R. (2012). The 11 April 2012 east Indian Ocean earthquake triggered large aftershocks worldwide. *Nature*, *490*(7419), 250–253. https://doi.org/10.1038/nature11504

Prejean, S. G., & Hill, D. P. (2014). Dynamic triggering of earthquakes. In *Encyclopedia of complexity and systems science* (pp. 1–36).

Price, S. F., Payne, A. J., Catania, G. A., & Neumann, T. (2008). Seasonal acceleration of inland ice via longitudinal coupling to marginal ice. *Journal of Glaciology*, *54*(185), 213–219. https://doi.org/10.3189/002214308784886117

Scholz, C. H. (2019). Mechanics of earthquakes. In *The mechanics of earthquakes and faulting* (pp. 207–237). Cambridge University Press.

Segall, P., & Matthews, M. (1997). Time dependent inversion of geodetic data. *Journal of Geophysical Research*, *102*(B10), 22391–22409. https://doi.org/10.1029/97jb01795

Selmes, N., Murray, T., & James, T. D. (2011). Fast draining lakes on the Greenland Ice Sheet. *Geophysical Research Letters*, *38*(15), L15501. https://doi.org/10.1029/2011GL047872

Sergienko, O. V. (2013). Glaciological twins: Basally controlled subglacial and supraglacial lakes. *Journal of Glaciology*, *59*(213), 3–8. https://doi.org/10.3189/2013JoG12J040

Stein, R. S. (1999). The role of stress transfer in earthquake occurrence. *Nature*, *402*(6762), 605–609. https://doi.org/10.1038/45144

Stevens, L. A., Behn, M. D., Das, S. B., Joughin, I., Noël, B. P. Y., van den Broeke, M. R., & Herring, T. (2016). Greenland Ice Sheet flow response to runoff variability. *Geophysical Research Letters*, *43*(21), 11295–11303. https://doi.org/10.1002/2016GL070414

Stevens, L. A., Behn, M. D., McGuire, J. J., Das, S. B., Joughin, I., Herring, T., et al. (2015). Greenland supraglacial lake drainages triggered by hydrologically induced basal slip. *Nature*, *522*(7554), 73–76. https://doi.org/10.1038/nature14480

Stevens, L. A., Hewitt, I. J., Das, S. B., & Behn, M. D. (2018). Relationship between Greenland Ice Sheet surface speed and modeled effective pressure. *Journal of Geophysical Research: Earth Surface*, *123*(9), 2258–2278. https://doi.org/10.1029/2017JF004581

Stevens, L. A., & Larochelle, S. (2024). Elastic stress coupling between supraglacial lakes (v1.2) [Dataset]. *Zenodo*. https://doi.org/10.5281/zenodo.10650188

Tedesco, M., Willis, I. C., Hoffman, M. J., Banwell, A. F., Alexander, P., & Arnold, N. S. (2013). Ice dynamic response to two modes of surface lake drainage on the Greenland ice sheet. *Environmental Research Letters*, *8*(3), 34007. https://doi.org/10.1088/1748-9326/8/3/034007

Tsai, V. C., & Rice, J. R. (2010). A model for turbulent hydraulic fracture and application to crack propagation at glacier beds. *Journal of Geophysical Research*, *115*(F3), F03007. https://doi.org/10.1029/2009JF001474

Ultee, L., Meyer, C., & Minchew, B. (2020). Tensile strength of glacial ice deduced from observations of the 2015 eastern Skaftá cauldron collapse, Vatnajökull ice cap, Iceland. *Journal of Glaciology*, *66*(260), 1024–1033. https://doi.org/10.1017/jog.2020.65

van der Veen, C. J. (1998). Fracture mechanics approach to penetration of surface crevasses on glaciers. *Cold Regions Science and Technology*, *27*(1), 31–47. https://doi.org/10.1016/S0165-232X(97)00022-0

van der Veen, C. J. (2007). Fracture propagation as means of rapidly transferring surface meltwater to the base of glaciers. *Geophysical Research Letters*, *34*(1), L01501. https://doi.org/10.1029/2006GL028385

Vaughan, D. G. (1993). Relating the occurrence of crevasses to surface strain rates. *Journal of Glaciology*, *39*(132), 255–266. https://doi.org/10.3189/S0022143000015926

Weertman, J. (1973). *Can a water-filled crevasse reach the bottom surface of a glacier?* IASH Publications.

Williamson, A. G., Willis, I. C., Arnold, N. S., & Banwell, A. F. (2018). Controls on rapid supraglacial lake drainage in West Greenland: An Exploratory Data Analysis approach. *Journal of Glaciology*, *64*(244), 208–226. https://doi.org/10.1017/jog.2018.8

Yang, K., & Smith, L. C. (2016). Internally drained catchments dominate supraglacial hydrology of the southwest Greenland Ice Sheet. *Journal of Geophysical Research: Earth Surface*, *121*(10), 1891–1910. https://doi.org/10.1002/2016JF003927

Yang, K., Smith, L. C., Chu, V. W., Gleason, C. J., & Li, M. (2015). A caution on the use of surface digital elevation models to simulate supraglacial hydrology of the Greenland Ice Sheet. *IEEE Journal of Selected Topics in Applied Earth Observations and Remote Sensing*, *8*(11), 5212–5224. https://doi.org/10.1109/JSTARS.2015.2483483

21699011, 2024, 5, Downloaded from https://agupubs.onlinelibrary.wiley.com/doi/10.1029/2023JF007481 by Test, Wiley Online Library on [27/06/2024]. See the Terms and Conditions (https://onlinelibrary.wiley.com/terms-and-conditions) on Wiley Online Library for rules of use; OA articles are governed by the applicable Creative Commons License

References From the Supporting Information

Green, A. E., & Sneddon, I. N. (1950). The distribution of stress in the neighbourhood of a flat elliptical crack in an elastic solid. In *Mathematical Proceedings of the Cambridge Philosophical Society* (Vol. 46, No. 1 pp. 159–163). Cambridge University Press.

Lai, C.-Y., Zheng, Z., Dressaire, E., Ramon, G. Z., Huppert, H. E., & Stone, H. A. (2016). Elastic relaxation of fluid-driven cracks and the resulting backflow. *Physical Review Letters*, *117*(26), 268001. https://doi.org/10.1103/PhysRevLett.117.268001

21699011, 2024, 5, Downloaded from https://agupubs.onlinelibrary.wiley.com/doi/10.1029/2023JF007481 by Test, Wiley Online Library on [27/06/2024]. See the Terms and Conditions (https://onlinelibrary.wiley.com/terms-and-conditions) on Wiley Online Library for rules of use; OA articles are governed by the applicable Creative Commons License